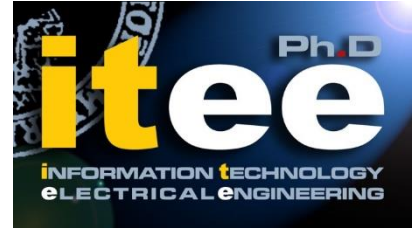




UNIVERSITÀ DEGLI STUDI DI NAPOLI  
**FEDERICO II**



**UNIVERSITÀ DEGLI STUDI DI NAPOLI FEDERICO II**

**PH.D. THESIS**

IN

**INFORMATION TECHNOLOGY AND ELECTRICAL ENGINEERING**

**LOW-COST TRANSDUCER  
NETWORK FOR REAL-TIME  
MOVEMENT TRACKING**

**DANIELE GATTI**

**TUTOR: PROF. PASQUALE ARPAIA**

**COORDINATOR: PROF. DANIELE RICCIO**

**XXXII CICLO**

**SCUOLA POLITECNICA E DELLE SCIENZE DI BASE  
DIPARTIMENTO DI INGEGNERIA ELETTRICA E TECNOLOGIE DELL'INFORMAZIONE**

TESI DI DOTTORATO

UNIVERSITÀ DEGLI STUDI DI NAPOLI “FEDERICO II”

DIPARTIMENTO DI INGEGNERIA ELETTRONICA  
E DELLE TELECOMUNICAZIONI

DOTTORATO DI RICERCA IN  
INFORMATION TECHNOLOGY AND ELECTRICAL ENGINEERING

---

LOW-COST TRANSDUCER  
NETWORKS FOR REAL-TIME  
MOVEMENT TRACKING

---

**DANIELE GATTI**

Il Coordinatore del Corso di Dottorato    Il Tutore

Ch.mo Prof. Daniele RICCIO

Ch.mo Prof. Pasquale ARPAIA

A. A. 2019–2020



# Abstract

In this thesis work, the main technologies and technique for the indoor positioning system (IPS) are discussed and presented. In particular, an alternative hybrid IPS and heading measurements system is being proposed. The hybrid navigation system is based on ultra-wideband technology, and on a twofold Ultrasonic (US) sensors for the heading measurements.

In the most application cases the, inertial measurements unit (IMU) measurements is combined with the IPS. Combining the two different systems, the position and orientation of a target can be tracked. In presence of static magnetic fields disturbance in the localization area, the magnetometer can not be used in the traditional IMU guidance system as a reference for the heading correction and measurements. For this reason, a new approach is proposed for measuring heading based on US and UWB fusing system.

The proposed system was prototyped and metrologically characterized, and then collocated in the *AugmenSur* project, an augmented reality application with the aim of providing real-time assistance to surgeon during the operating and training phases.



# Contents

<b>Abstract</b>	<b>i</b>
<b>List of Acronyms</b>	<b>v</b>
<b>List of Tables</b>	<b>vii</b>
<b>List of Figures</b>	<b>xiii</b>
<b>Introduction</b>	<b>xv</b>
<b>1 State of the art</b>	<b>1</b>
1.1 Indoor positioning system . . . . .	1
1.1.1 Localization algorithm . . . . .	2
1.1.2 Localization parameter extraction . . . . .	10
1.2 Localization technologies and application . . . . .	16
1.2.1 Radio frequency . . . . .	16
1.2.2 Infrared . . . . .	20
1.2.3 Ultrasonic . . . . .	21
1.2.4 Other . . . . .	24
1.3 Positioning tracking system for surgery application . . . . .	25
1.3.1 Optical Tracker . . . . .	26
1.3.2 Magnetic Tracker . . . . .	27
<b>2 Proposed Method</b>	<b>29</b>
2.1 Conventional heading measurements System . . . . .	29
2.2 The Ultrasonic heading System . . . . .	32
2.2.1 Measuring principle . . . . .	33
2.2.2 Sine-Fit based phase difference extraction algorithm	36
2.3 First prototype Ultrasonic IPS . . . . .	40

---

2.3.1	Beacon node recognition criteria . . . . .	40
2.3.2	Transmitter node . . . . .	42
2.3.3	Receiver node . . . . .	42
2.3.4	Localization algorithm . . . . .	44
2.3.5	Experimental results . . . . .	47
2.4	UWB based proposal IPS . . . . .	48
2.5	Simulation results . . . . .	51
<b>3</b>	<b>Results</b>	<b>55</b>
3.1	Ultrasonic Heading prototype . . . . .	55
3.1.1	Ultrasonic transmitter . . . . .	56
3.1.2	Receiver node . . . . .	59
3.1.3	Realization . . . . .	62
3.2	Low cost electronic goniometer . . . . .	62
3.2.1	Realization . . . . .	63
3.2.2	Metrological characterization . . . . .	64
3.3	Metrological characterization . . . . .	67
3.3.1	Metrological results . . . . .	70
3.3.2	Noise and distortion analysis . . . . .	72
3.3.3	Interference Analysis . . . . .	73
3.3.4	Throughput Performance . . . . .	78
<b>4</b>	<b>Conclusions</b>	<b>81</b>
	<b>Bibliography</b>	<b>84</b>

# List of Acronyms

- 3pSF** three parameters sine fitting. 36, 37, 55, 61, 67, 72, 77
- ADC** Analog Digital Converter. 72, 77
- AoA** Angle of Arrival. ix, 10, 12, 13, 21, 34
- AWGN** Additive White Gaussian Noise. 51
- EG** Electronic goniometer. 63, 64, 66, 67, 69, 71
- EKF** Extended Kalman filter. xi, xvi, 49–53
- ENOB** Effective-Number-Of-Bit. vii, 72, 73
- FBN** fixed beacon node. 1, 2
- FR** reference frame. 1, 33, 35, 36, 51, 52
- GPS** Global Positioning System. xv, 1
- IMU** inertial measurements unit. i, xv, 29, 31, 32, 82, 83
- IPS** indoor positioning system. i, ix, xv, 1, 16, 18, 20, 21, 24, 25, 47, 49
- IR** Infrared. x, 13, 20, 21, 25, 26
- LF** localized frame. x, xi, 33, 35, 36, 51
- LOS** line of sight. xv, 6, 14, 22
- MEMS** Micro Electro-Mechanical Systems. 29, 30, 55, 59, 61

- NLOS** none line of sight. 14, 15
- OP** operational amplifier. 43, 61, 62
- PCB** Printed Circuit Board. xi, 48, 62
- RF** Radio Frequency. 11, 13, 16, 22, 24, 25
- RFID** Radio Frequency Identification. ix, 3, 18, 25
- RSSI** Received Signal Strength Indicator. ix, 3, 4, 13, 16–19
- SNR** Signal to Noise Ratio. vii, 51, 72, 73
- SPL** Soun Pressur Level. xi, 57–61, 77
- TDeA** time difference extraction algorithm. 40
- TDoA** Time Differential of Arrival. 10–12, 19–24, 34, 36, 38, 40, 44–47
- THD** Total Harmonic Distortion. vii, 61, 72
- ToF** Time of Flight. 10, 21, 22, 48
- UHS** ultrasonic heading system. xvi, 32, 67, 70–72, 74
- US** Ultrasonic. i, x–xii, xv, xvi, 11, 13, 24, 32–36, 40, 41, 47, 51, 55, 56, 58, 59, 61, 62, 67–70, 74
- USr** ultrasonic sensor receiver. 32–34, 36, 37, 51, 55, 59, 61, 73, 74, 77
- UWB** ultra-wide-band. i, ix, xi, xv, xvi, 19, 47, 48, 51, 82

# List of Tables

2.1	Time difference extraction. . . . .	39
2.2	Measurements results. . . . .	47
3.1	THD, SNR, ENOB varying the number of bits and sampling rate when the reference angle $\theta_{ref} = 0$ [deg] . . . . .	72
3.2	The polynomials fitted coefficients for the Prowave 250ST160 points of the attenuation function in Fig.3.16. Half of the total attenuation angle was considered ( $\phi$ [0:90] deg . . . . .	76
3.3	Comparison among the proposed system and recent state-of-the-art solutions considering the angular range, the maximum operating distance, and the maximum error. . .	77



# List of Figures

- 1.1 The localization process schematization. The extracted parameters depends on the localization algorithm technique. 2
- 1.2 The pRFID are stimulated by the reader antenna. The presence of human modified the RSSI [1]. . . . . 3
- 1.3 Circle intersection example. Three beacons  $B_{1,2,3}$  are considered and one target  $T$ . The angle  $\theta_{12}, \theta_{13}, \theta_{23}$ , are computed from the beacons angle measurements. . . . . 4
- 1.4 The trilateration geometrical problem. Three beacons  $B_{1,2,3}$  and one target  $T$  are considered. The distance  $|d_{1t}|, |d_{2t}|, |d_{3t}|$ , represents the circles radius. The circles are centered in the beacons. . . . . 6
- 1.5 Qualitative noising distance measurements effects for the position estimation performed by the trilateration algorithm. Two intersection region  $T$  and  $T^*$  are presents. . . 7
- 1.6 The target receiving the  $B_1$  signal, the  $B_2$ , and finally the  $B_3$  signal. . . . . 11
- 1.7 AoA measurements principle configuration. The AoA is measured with respect to the beacons-line intersection. . . 13
- 1.8 Two ray model path schematization [2]. . . . . 16
- 1.9 Indoor positioning system, based on two low-frequency coupled resonant antennas and the trilateration algorithm: the received and transmitted loop antenna are schematics with equivalent LC circuit [3]. . . . . 17
- 1.10 The RFID reader and tag used in LANDMARC IPS [4] . 18
- 1.11 Block diagram of UWB movement detection system [5]. . 19
- 1.12 The 2016 HTC Vive beacon laser-scan and the headset. . 21
- 1.13 Cricket unit with sensor-board, working as either a beacon or a listener [6]. . . . . 22

1.14	Devantech wall-mounted ultrasonic sensor. Two separate ultrasonic sensors were used, one for transmitting the ultrasonic burst and another for receiving the corresponding echo [7]. . . . .	23
1.15	System devices: (a) Acoustic Beacons and Gateway, (b) Mobile Device based on a iPhone 4S [8]. . . . .	24
1.16	Example of reflectors markers visualization in the IR spectrum. . . . .	26
1.17	Electromagnetic tracking setup for surgical navigation. A head-mounted transmitter allows to control an instrument during sinus surgery [9]. . . . .	27
2.1	(a) Row magnetometer measurements values for the 3-axis, noting the bias and eccentricities presence in the measurements. (b) Calibrated and normalized magnetometer value. . . . .	30
2.2	Pitch, roll, and yaw representation. . . . .	32
2.3	The initial condition for orientation, velocity and position indicated respectively with $\overline{O}_0$ , $\overline{V}_0$ , $\overline{P}_0$ . The orientation information, combined with the acceleration measurements, are needed to compute the true Body acceleration. . . . .	33
2.4	The angle $\theta^*$ is the positive heading (yaw) angle of the localized frame ( $X^*$ , $Z^*$ ) with respect to the reference frame ( $X$ , $Z$ ). . . . .	33
2.5	The received plane wave signal. The heading angle $\theta^*$ is related to the $\delta_{us}$ distance measurements. . . . .	34
2.6	Generic angle projection. The $\beta_{bias}$ correction term depends on the US relative emitter-LF position. . . . .	35
2.7	Time difference extraction for the same signal slope: (i) wrong ( $\bullet$ ), directly by eq. (2.19), $\delta t_{phase} = -37.5 \mu s$ ; and (ii) correct ( $\blacklozenge$ ), by the proposed algorithm, $\delta t_{algo} = 2.43 \mu s$ . . . . .	38
2.8	Real damped response of the <i>SensComp's Series 9000</i> ultrasonic sensors, stimulated by a $f_4 = 40 kHz$ , $10 V_{pp}$ single burst signal (sample frequency $f_s = 1 MHz$ ). . . . .	41
2.9	Transmitter beacon node: (A) the low-power signal coupling transformer, and (B) the ultrasonic sensor <i>SensComp's Series 9000</i> . . . . .	42

2.10	Receiver node: (A) the ultrasonic sensor <i>SensComp's Series 9000</i> , (B) the microcontroller Nucleo STM32 L152RE, and (C) the board custom circuit. . . . .	43
2.11	Geometrical 2D problem representation (A, B, and C: beacons; and T: target generic position). . . . .	44
2.12	2-Beacons case study: specific case of symmetric positions with respect to the axis $y$ . . . . .	45
2.13	The <i>DecaWaveDW1000</i> module with custom PCB interface circuits. . . . .	48
2.14	The two-way ranging timing and operation schematization. . . . .	49
2.15	Triangulation problem in 2D. . . . .	50
2.16	The measurements chain. Fusing the UWB position measurements and the US heading information the position and orientation of the LF are known. . . . .	51
2.17	Heading estimation mean error and standard deviation bar plot. . . . .	52
2.18	Matlab <sup>®</sup> EKF simulation result for $\beta_{bias}$ and positioning estimation. The reference position in (*) and the EKF position estimation (·) points. . . . .	53
2.19	Plot of the beta bias error considering the same position data computed in the 2.18. . . . .	54
3.1	The Prowave 250ST160 module of the measured impedance. The minimum module of the impedance is $ Z  = 0.75 \text{ k}\Omega$ at $f_r = 25.4 \text{ kHz}$ . . . . .	56
3.2	The Prowave 250ST160 SPL referred to $0.0002 \mu\text{bar}$ for $10 \text{ V}_{rms}$ at $30 \text{ cm}$ considering different driving frequency. The maximum of the SPL is at the resonance frequency ( $25 \text{ kHz}$ ) [10]. . . . .	57
3.3	The estimated SPL Prowave 250ST160 emitter, varying the sensor distance considering $V_{dr} = 2.83 \text{ V}_{rms}$ driving voltage. The SPL was estimated thanks to the transducer supplier information. . . . .	58
3.4	The SPU0410LR5H sensitivity response normalized to 1 kHz [11]. The increase in sensitivity at $f_r = 25 \text{ kHz}$ with respect to the normalized frequency is equal to $10.4 \text{ dBV/Pa}$ . . . . .	60
3.5	The SPU0410LR5H estimated receiving rms output voltage considering the Prowave 250ST160 emitter driven by a $V_{dr} = 2.83 \text{ V}_{rms}$ . . . . .	61

3.6	The single channel analog filter and voltage reference circuits schematics. The same circuit was duplicate for the second sensor. . . . .	62
3.7	The filtering and transducer complete board. The total size of the filtering board can be halved if BNC connectors are removed . . . . .	63
3.8	The plate and the potentiometer goniometer prototype. The plate can rotate in clockwise and anticlockwise, in this way an arbitrary heading angle can be chosen for the measurements. . . . .	64
3.9	(a) Measured resistance point and the linear regression. (b) Percentage deviation. . . . .	65
3.10	Mechanical setup: a) the transducer board on the rotating plate of the reference goniometer, b) the US beacon on the Plexiglas support, and c) the transducer board sliding along a grooved bar at different distances from the beacon. . . . .	66
3.11	The measurements station in details: the receivers board mounted on the rotating plate (1), the US transmitter (2), the DSO (3), the waveform generator (4), the ohmmeter (5). The instruments where controlled by a custom Matlab <sup>®</sup> application. . . . .	67
3.12	Assumptions for US transmitter and receiver: alignment of the origins of the reference frame $(X, Z)$ and localized frame $(X^*, Z^*)$ . A positive heading $\theta^*$ of the localized frame is sketched. . . . .	68
3.13	Calibration of the US heading system (mean and $1-\sigma$ repeatability bar plot) for a beacon-receiver distance of 1.0 m. . . . .	69
3.14	The measurements scenario block diagrams. . . . .	70
3.15	(a) The percentage deterministic error versus the measured angle for a beacon-receiver distance of 1.0 m. (b) $1-\sigma$ percentage repeatability versus the measured angle for a beacon-receiver distance of 1.0 m. . . . .	71
3.16	The Prowave 250ST160 attenuation functions provided by the supplier $(\cdot)$ [10] and, the fitted function $(-)$ . The attenuation was measured considering the reference distance and driving emitter voltage and rotating the emitter by an angle $(\phi)$ . . . . .	74

- 
- 3.17 The direct and the reflected path and the reflected angle ( $\theta_r$ ). The reflected angle was computed apply the Snell's law. The emitter attenuation related to the ( $\phi$ ) angle and the attenuation function (Fig.3.16). . . . . 75
- 3.18 Incident angle  $\theta^\#$  of reflected wave at varying heading angle for  $\theta^*$  equal to -35 deg (a), 0 deg (b), 25 deg (c). Deterministic error caused by interference depends on directivity of the receiver and the difference of the paths between the two reflected waves from beacon to receivers ( $\Delta_{Path}$ ). In (d), the Matlab<sup>®</sup> simulation plots of the deterministic error as a function of interference amplitude (y axis) and phase shift (x axis) is reported. The latter is equivalent to  $\Delta_{Path}$ . White line indicates deterministic error of 1.2 deg. Black dots indicate the simulated errors at varying  $\theta^*$  within the range [-35, 25] deg, with a receiver-beacon distance of 1 m, and both of them 3 m far from a lateral wall. . . . . 78



# Introduction

The indoor positioning system (IPS) is a system adopted to solve the problem of localization and identification of a targets of interest in closed environments. The existing outdoor technology (i.e. Global Positioning System (GPS)) is bounded to limited performances in indoor applications. The big disadvantage with the GPS is that the receiver needs a line of sight (LOS) for at least four satellites in the sky. Inside buildings or in other cases where there are obstructions between the GPS receiver and the satellites, the accuracy is too low for most indoor environments application.

The development and the application of the IPS increased radically in the last few years and then, the research interest as well. For instance, they are used in navigation, health care, logistics, in-home asset tracking, emergency services, visitor identification, security, robot navigation and cooperation [12].

Different IPS exist, implemented with a different positioning techniques, technologies and performance. There are IPS with millimetre accuracy, but they are so expensive that few applications can afford them. The current research interest is focus on solving specific property of the IPS related to the specific application, in order to reduce the cost and optimize the performance.

In the first chapter, the IPS technologies and application are presented. In the second, the proposed method is exposed. Finally, in the third chapter, the prototype realization and performance are presented and discussed. The proposed system is able to measure the position and heading of a target fusing the UWB and US technologies. In the most application cases the inertial measurements unit (IMU) is combined with the IPS. Combining the two different systems, the position and orientation of a target can be tracked.

Traditional IMU-based guidance and tracking system exploit data

fusion from accelerometer, gyroscope, and magnetometer in order to measure the orientation and position for a short time due to the drift problem. Accelerometers are used to compensate the gyroscope drift for the pitch and roll static orientation. The magnetometer is used for the static yaw angle estimation and for the dynamic assessment of all angles. However, magnetometer fails in magnetic harsh conditions.

The proposed method, is a free-magnetometer heading estimation, based on the UWB location system and the US measurements. The UWB was used for the distance measurements and then the position was computed by the trilateration technique combined with an Extended Kalman filter (EKF). The heading was computed measuring the phase-shift of two received US signals apply the sine-fit algorithm. Finally, the proposed system is was prototyped and metrologically characterized.

The proposed ultrasonic heading system (UHS) was in the *AugmenSur* project. AugmenSur, is an augmented reality application with the aim of providing real-time assistance to surgeon in the operating and training phases. The application provides information to the surgeon during the operation and allows him/her to work with his hands free. The surgeon head movement tracking guarantees to work leaving both hands free and the application user interaction, so the surgeon is able to navigate in the application menu. The metal instruments and equipment close to the surgeon, caused a degradation of the magnetometer performance. For this reason, the heading movement is measured by the US proposed UHS.

# Chapter 1

## State of the art

### 1.1 Indoor positioning system

An indoor positioning system (IPS) is a system able to measure a target position with respect to an orthogonal coordinate reference system, the reference frame (FR). The reference frame is fixed and represent the space where the target can be in place [13]. It include the fixed beacon node (FBN). The main purpose of the FBN is to measure the target distance with respect to it self.

Many application needs to know the dynamic target position such as: domotics, augmented reality [14, 15, 16], robotics [17, 18, 19], assisted navigation in buildings [20, 21], health systems [22, 23], and objects localization [24, 25]. Any application required different characteristics of the IPS. The most important features of an IPS accuracy, latency, and range. Usually, the accuracy range in indoor localization application varies from 1 m to sub-centimeter range.

Others important characteristics are the scale and scalability, the power consumption, cost. The scale is the coverage area per FBN unit of infrastructure. The scalability measures how easy is it to expand the FBN by physical coverage or by adding more target. The latency range varies from a few ms to seconds.

In general, the outdoor localization technologies are not applicable to indoor environments due to the low accuracy. For instance, in [26], a classical outdoor positioning approach is implemented, by exploiting in particular GPS and an Inertial Measurement Unit (IMU) embedded in a smart phone, for indoor pedestrian tracking with an average loca-

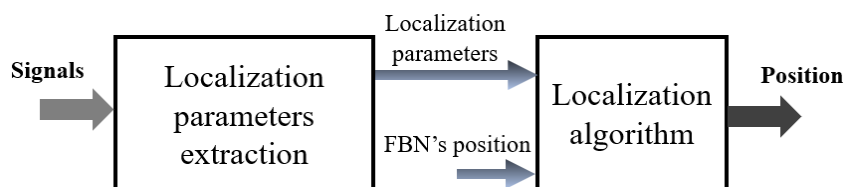


Figure 1.1. The localization process schematization. The extracted parameters depends on the localization algorithm technique.

tion uncertainty of 1.35 m. Such a high uncertainty level is due to the fact that the GPS receives signals from multiple satellites and employs a triangulation process to determine physical locations, but the signals are heavily attenuated and reflected by the building materials. Different technologies and techniques were required for the indoor tracking application.

The localization problem is faced through two main steps: the FBN-localized target distance measurement and the localization algorithm. The localization algorithm inputs are the FBN-target distance or the relative angle and the FBN position (it depends on the localization technique). The target position with respect to the reference frame is the output localization algorithm.

In general, wave signal is exchanged between the FBN and the target in order to estimate the distance or the relative angle and, in general the localization parameters. The wave signal physics depends on the FBN and target realization technology. The localization process can be summarize as sketched in the Fig.1.1.

### 1.1.1 Localization algorithm

Different localization algorithm exist in literature. The most common are the: *Triangulation*, *Trilateration and multilateration*, *Scene analysis*, and *Proximity localization*.

- **Proximity localization.** The proximity based positioning technique, recognize when a target is “near”, or in proximity to a known position. Usually, this technique is used for the objects or person localization [24, 25] with low Accuracy and low frame rate, guaranteeing low power consumption.

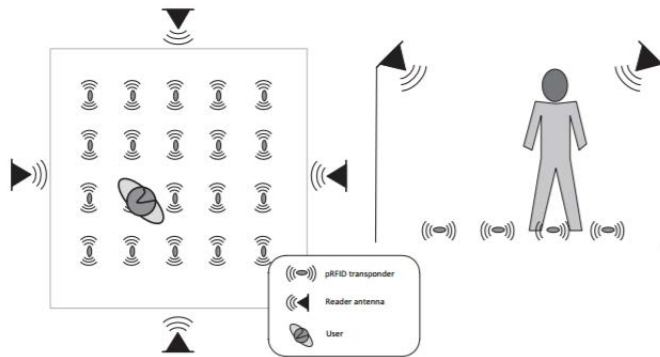


Figure 1.2. The pRFID are stimulated by the reader antenna. The presence of human modified the RSSI [1].

An example of proximity based positioning system was presented in [1]. The Authors extract the radio tomographic imaging using a passive Radio Frequency Identification (RFID). The system uses a passive RFID transponder mounted on the floor of a room, and powered over the electromagnetic communication signals transmitted by a few reader antennas in the room edges. The difference between transmitted and received signal power, can be used as physical measurement basis for human localization algorithms. In Fig.1.2, the system architecture is shown. The maximum error is 45 cm in a  $5\text{m} \times 5\text{m}$  area, considering three people localization target.

Actually, this technique does not estimate the position of the target, but defines the geometrical area in the reference frame space, where the location of the target is.

- **Scene analysis.** Scene analysis refers to an algorithms based on collected features (fingerprints) of a scene and then to the estimation of a target location. The target location estimation is achieved by finding the closest location of the online measurements with respect to the offline fingerprint information.

In general, the fingerprints location process is composed by two phases: the offline training phase and the online location target estimation. During the offline phase, the positioning database is stored. The positioning database can be constructed using

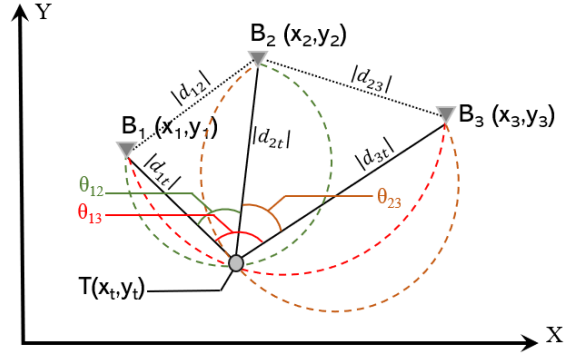


Figure 1.3. Circle intersection example. Three beacons  $B_{1,2,3}$  are considered and one target  $T$ . The angle  $\theta_{12}$ ,  $\theta_{13}$ ,  $\theta_{23}$ , are computed from the beacons angle measurements.

marks at known positions and extracting the corresponding features. A common feature used for fingerprints is the Received Signal Strength Indicator (RSSI). During the the online phase, the feature of the observed signal (e.g. RSSI) is matched with each sample of the positioning database. The matching criteria can be, for instance, a probabilistic methods (e.g.K-Means clustering [27]), a neural network based method (e.g. [28]) or in general in an optimization problem. We can define a cost function  $f_c$  where the input domain is the fingerprints positioning database  $Fp_{DB}(k)$ , and the observed signal named  $Os$ .

The position estimated  $P_e$  in the reference sampled space  $K$ , can be written as:

$$P_e = \underset{k \in K}{\operatorname{argmin}} f_c(Fp_{DB}(k), Os) \quad (1.1)$$

The minimization problem in eq.(1.1) can be solved using different techniques. The main challenge of the RSSI based scene analysis technique, is that the received signal strength could be affected by diffraction, reflection and multipath when propagating in indoor environments occurs.

The accuracy of the scene analysis technique depends generally on the granularity and distribution of the fingerprinted location.

- **Triangulation.** The triangulation technique is based on geometric and trigonometric properties. The localization parameters are the angular distance between the nodes. A classical triangulation technique is the circle intersection [29]. In Fig.1.3, the geometrical localization problem is sketched. The three fixed beacons  $B_{1,2,3}$  position and the relative distance  $|d_{12,23,13}|$ , are known.

Applying the law of cosine from the triangle between the target  $T$  and the beacons  $B_{1,2}$ , the following equation can be write:

$$|d_{12}|^2 = |d_{1t}|^2 + |d_{2t}|^2 - 2|d_{1t}| |d_{2t}| \cos \theta_{12} \quad (1.2)$$

The terms  $|d_{1t}|$  and  $|d_{2t}|$ , are the distance between the target  $T$  and the beacons  $B_{1,2}$ .

Considering three beacons, a system of three equations can be written in order to determine the distance  $|d_{1t,2t,3t}|$ . Applying the law of cosine to all pairs of beacons:

$$\begin{cases} |d_{13}|^2 = |d_{1t}|^2 + |d_{3t}|^2 - 2|d_{1t}| |d_{3t}| \cos \theta_{13} \\ |d_{12}|^2 = |d_{1t}|^2 + |d_{2t}|^2 - 2|d_{1t}| |d_{2t}| \cos \theta_{12} \\ |d_{23}|^2 = |d_{2t}|^2 + |d_{3t}|^2 - 2|d_{2t}| |d_{3t}| \cos \theta_{23} \end{cases} \quad (1.3)$$

The non linear system of equation (1.3) can be solved using, for instance, the least squares method (LSQ). The target position  $(x_t, y_t)$  can be expressed in function of the distance  $|d_{1t}| |d_{2t}|$ :

$$\begin{cases} |d_{1t}|^2 = (x_t - x_1)^2 + (y_t - y_1)^2 \\ |d_{2t}|^2 = (x_t - x_2)^2 + (y_t - y_2)^2 \\ |d_{3t}|^2 = (x_t - x_3)^2 + (y_t - y_3)^2 \end{cases} \quad (1.4)$$

Subtracting third equation from the first and the second, the linear equations in the  $x_t$  and  $y_t$  unknowns system can be found:

$$\begin{cases} |d_{3t}|^2 - |d_{1t}|^2 = x_1^2 - x_3^2 + 2(x_1 - x_3)x_t + \\ \quad y_1^2 - y_3^2 + 2(y_1 - y_3)y_t \\ |d_{3t}|^2 - |d_{2t}|^2 = x_2^2 - x_3^2 + 2(x_2 - x_3)x_t + \\ \quad y_2^2 - y_3^2 + 2(y_2 - y_3)y_t \end{cases} \quad (1.5)$$

Finally, the target position  $(x_t, y_t)$  can be easily computed from

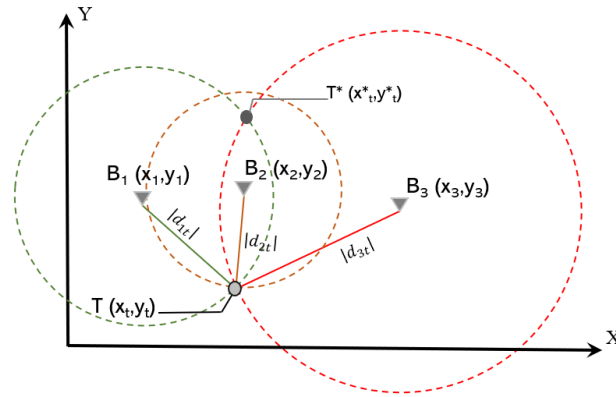


Figure 1.4. The trilateration geometrical problem. Three beacons  $B_{1,2,3}$  and one target  $T$  are considered. The distance  $|d_{1t}|$ ,  $|d_{2t}|$ ,  $|d_{3t}|$ , represents the circles radius. The circles are centered in the beacons.

the eq.(1.5).

The geometric circle intersection is widely used in literature. This technique fails when the three beacons and the target lie on a same circle.

Several triangulation algorithms exist in literature: Geometric Triangulation, Iterative Search, Newton-Raphson [29]. The geometric triangulation is based on the law of sine and works consistently, only when the target is within the triangle formed by the three beacons. There is an improved version which does not require beacon ordering and works over the whole navigation plane. The target can be localized in different areas served by different beacons. Nevertheless, there are few determined lines where localization is not possible [30]. The Newton Raphson is hard to solve because the problem equations are non-linear.

The trinagulation technique offer good performance in a limited space, due to the ease of establishing stations at appropriate distances and ascertaining the line of sight (LOS).

- **Trilateration and multilateration.** The trilateration is a technique based on range-anchor distance measurements. The target position is computed using geometry and in particular, the properties of circles and spheres. The beacons-target distances repre-

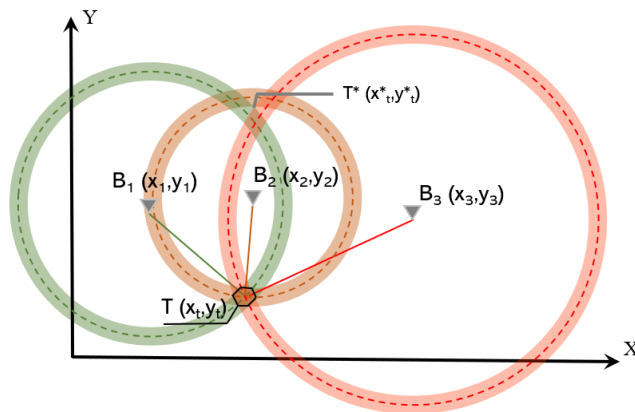


Figure 1.5. Qualitative noising distance measurements effects for the position estimation performed by the trilateration algorithm. Two intersection region  $T$  and  $T^*$  are presents.

sent the circle radius and the beacon represents the circle center. The circle intersection is the target location. Considering an  $N$ -dimensional space,  $N + 1$  beacons is needed in order to localize properly the target. If the number of beacons taken into account is greater than the minimum needs, the trilateration becomes a multilateration.

For instance, considering a 2D localization space, three beacons were needed in order to localize the target. In Fig.1.4, the geometrical configuration is sketched. Assuming only two beacons  $B_{1,3}$ , the circles in red and green have two intersection:  $T(x_t, y_t)$  and  $T^*(x^*_t, y^*_t)$ . Introducing a third circle (red circle), the target is correctly localized at the coordinate position  $(x_t, y_t)$ . The target position  $(x_t, y_t)$  can be easily computed from the eq. (1.4).

The distance measurements are effected by uncertainty and then each circumference has an uncertainty area associated [31]. In Fig.1.5 a noisy distance measurements effect in the position estimation is sketched. The target position can be in the polygonal black zone and in the  $T^*$ , with a different probability. The circle intersection will not result in a single point, but in an area of uncertainty.

Different possible solutions are present in the literature, for in-

stance the *Nonlinear Least Squares Multilateration*, *Linear Least Squares Multilateration*, the *adapted multilateration* [32].

Considering  $N$  beacons, the system multilateration equations is the follow:

$$\begin{cases} |d_{1t}|^2 = (x_t - x_1)^2 + (y_t - y_1)^2 \\ |d_{2t}|^2 = (x_t - x_2)^2 + (y_t - y_2)^2 \\ \dots \\ |d_{Nt}|^2 = (x_t - x_N)^2 + (y_t - y_N)^2 \end{cases} \quad (1.6)$$

- The *Nonlinear Least Squares Multilateration* solve the non linear multilateration equations by using a LSQ method. Assuming  $N$  beacons in a fixed positions at  $B_n = (x_n, y_n)$  and  $|d_{nt}|$  distance measurements with  $n \in N$ , from the target node in the position  $T(x_t, y_t)$ , the LSQ finds the most likely position of the target, denoted by  $\hat{T}$ .

The LSQ minimizing the sum of the squared residuals between the observed ranges  $|d_{nt}|$ , and the estimated distance  $\|T - B_i\|$ :

$$\hat{T} = \underset{T}{\operatorname{argmin}} \sum_{n=1}^N (\|T - B_n\| - |d_{nt}|)^2 \quad (1.7)$$

The minimization problem can be solved, for instance, applying the Newton type optimization algorithms. The Newton optimization algorithms are a class of iterative algorithm. It starts from an initial guess solution and then, does a number of iterations. Each iteration gradually improves the estimated position until a local minimum of the objective function in eq.(1.7) is obtained.

- The *Linear Least Squares Multilateration* is based on a linear arrangement of the eq.(1.6). The equation (1.6) can be linearized by subtracting one of the equations from the remaining  $N - 1$  (similar in the eq.(1.4) and (1.5)). A linear form can be found:

$$AT^T = Y \text{ where :} \quad (1.8)$$

$$Y = \frac{1}{2} \begin{bmatrix} x_1^2 - x_N^2 + y_1^2 - y_N^2 + |d_{Nt}|^2 - |d_{1t}|^2 \\ x_2^2 - x_N^2 + y_2^2 - y_N^2 + |d_{Nt}|^2 - |d_{2t}|^2 \\ \vdots \\ x_{N-1}^2 - x_N^2 + y_{N-1}^2 - y_N^2 + |d_{Nt}|^2 - |d_{(N-1)t}|^2 \end{bmatrix}$$

$$A = \begin{bmatrix} x_1 - x_N & y_1 - y_N \\ x_2 - x_N & y_2 - y_N \\ \vdots & \vdots \\ x_{N-1} - x_N & y_{N-1} - y_N \end{bmatrix}$$

This linear regression problem is solved by the closed form solution:

$$\hat{T} = (A^T \cdot A)^{-1} A^T Y \quad (1.9)$$

To avoid trapping into local minimum when using not linear method, the linear solution is usually a starting point for the non linear iterative optimization process, because the linear estimation lies in the global minimum [33].

- The *adapted multilateration* approach tries to estimate the target position using circle intersections. Furthermore, adapted multilateration aims to reduce the computational overhead involved with matrix calculations in LSQ based methods.

This solution consists of three steps: *intersection and elimination*, *first estimation* and *refinement*.

In the first step two *intersecting* circles are arbitrarily chosen. The circles may intersect at one or two points. If there is more than one point, the location with the larger distance to the third beacon is *deleted*.

In the *first estimation* step, the previously computed intersection point is moved to the middle of the line connecting itself to the closest point of the third beacons circle. In order to compensate the errors introduced by the ranging measurements. The calculation results using the resemblance of triangles.

In the last step the position can be further *refined*. Therefore, the anchors that were not used in the previous steps are added to the position estimation process according to the same principle used in the second step.

### 1.1.2 Localization parameter extraction

In the section 1.1, the localization parameters concept were introduced. The parameters are related to the *localization algorithm* features. The most important parameter extraction technique can be summarized in: *time based* and *signal analysis*.

- **Time based.** The principal time based parameter extraction technique, such as: *Time of Flight (ToF)*, *Time Differential of Arrival (TDoA)*, *Angle of Arrival (AoA)*. The time based measurements is founded on the signal velocity information and travel time from the beacons to the target or vice versa.
  - The (ToF) measure the beacon-target distance by measuring the propagation time of the signal travelling from one to the other. The n-th beacon-target distance  $d_{nt}$  is equal to:

$$d_{nt} = v t_{nt} \quad (1.10)$$

Where  $v$  is the signal speed and  $t_{nt}$  the n-th signal travel time. The signal speed is related to the signal nature, the  $t_{nt}$  can be measured in different way. Two principal ways exist to calculate this distance: the *one-way* and the *two-way*.

In the *one-way* techniques only the beacons or the target, send a signal packet to the receiving node. In the *two-way* techniques, the beacons and the target send and receive a signal packet. The ToF require time synchronization between the nodes (beacons, target) [34].

The problem of synchronization in a network of n nodes, corresponds to the problem of matching the clock of the different nodes. The clock is a timer that counting the oscillations of a quartz crystal. The clock is used to synchronize digital electronic devices providing an accurate, stable and reliable time reference. Actually, despite their high stability, quartz crystals present on the nodes of a distributed system, oscillate at frequencies slightly different, and gradually the clocks difference diverge over the time (clock-skew), pulling away the clock values between them (clock-drift) [35]. The nodes synchronization is needed in order to compute the  $t_{nt}$ .

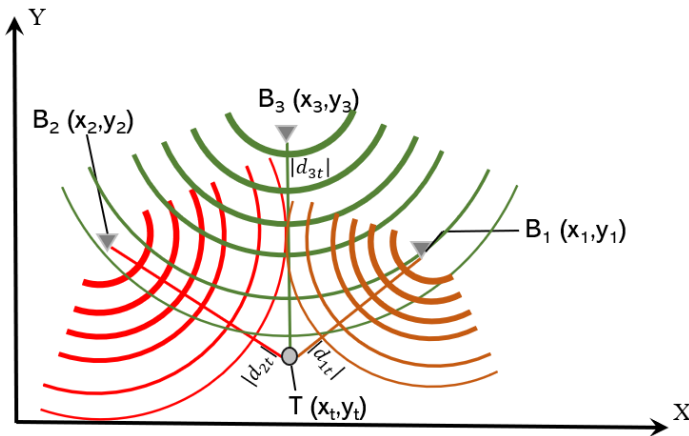


Figure 1.6. The target receiving the  $B_1$  signal, the  $B_2$ , and finally the  $B_3$  signal.

A pair of different signal e.g Ultrasonic (US) and Radio Frequency (RF) with high different speed can be used in the ranging evaluation; in this way only the beacons synchronization is needed. This technique is the time difference of arrival. The time difference at the receiver node is:

$$t_1 - t_2 = \frac{d_{nt}}{v_1} - \frac{d_{nt}}{v_2} \quad (1.11)$$

the terms  $v_2$  is the highest speed signal:  $v_2 \gg v_1$ . Assuming the  $t_2$  as the starting timer counter, the beacons-target distance is equal to [6]:

$$d_{nt} \approx v_1 t_1 \quad (1.12)$$

- The (TDoA) technique measures the times of arrival from a target on two distinct beacons. Each beacon emits a synchronous signal to the target. The target registers each received signal instant from the different beacons. This technique does not require a target beacons time synchronization. The first receiver signal determine the starting point of the counting process. The following received signal from the oth-

ers beacons complete the TDoA calculation. The first received signal is used to synchronize the next timing measurements. In Fig. 1.6, considering the  $t_{1,2,3}$  arrival time, combining the equation (1.6) with the equation (1.10) the follow equation can be written:

$$\begin{cases} v t_1 = \sqrt{(x_t - x_1)^2 + (y_t - y_1)^2} \\ v t_2 = \sqrt{(x_t - x_2)^2 + (y_t - y_2)^2} \\ v t_3 = \sqrt{(x_t - x_3)^2 + (y_t - y_3)^2} \end{cases} \quad (1.13)$$

Subtracting the second and third equation from the first, the target position is function of the time difference:

$$\begin{cases} v \delta_{21} = \sqrt{(x_t - x_2)^2 + (y_t - y_2)^2} - \sqrt{(x_t - x_1)^2 + (y_t - y_1)^2} \\ v \delta_{31} = \sqrt{(x_t - x_3)^2 + (y_t - y_3)^2} - \sqrt{(x_t - x_1)^2 + (y_t - y_1)^2} \end{cases} \quad (1.14)$$

The  $\delta_{21}$  is the TDoA between the  $t_1$  and  $t_2$ . The equations (1.14) represent two hyperbolas, the beacons  $B_{21}$  represent the foci of the one and the beacons  $B_{31}$  the foci of the second one. The two hyperbolas intersection is the target position  $(x_t, y_t)$ . Two solution for the equation system in (1.14) exist in order to obtain an unique solution, another beacons must be introduce in the configuration. Usually the correlation analysis provides the time delay corresponding to the difference in the signal path [36].

- The AoA technique measure the angle formed by the receiver-transmitted signal or vice versa, with respect to a reference plane. Usually the beacons-received signal angle is measured. Generally the AoA is measured using sensors array [37].

In Fig.1.7, the geometrical configuration for two beacons and one target was sketched. For this configuration, the target emits the signal, and the angle formed by the beacons can be measured. The AoA  $\theta_{1t}$  is related to the distance  $\delta_d$  and the known distance  $|d_{12}|$ :

$$|d_{12}| = \delta_d \cos \theta_{12} \quad (1.15)$$

The most common way to measure the distance  $\delta_d$  is the TDoA technique. The TDoA with respect to the two bea-

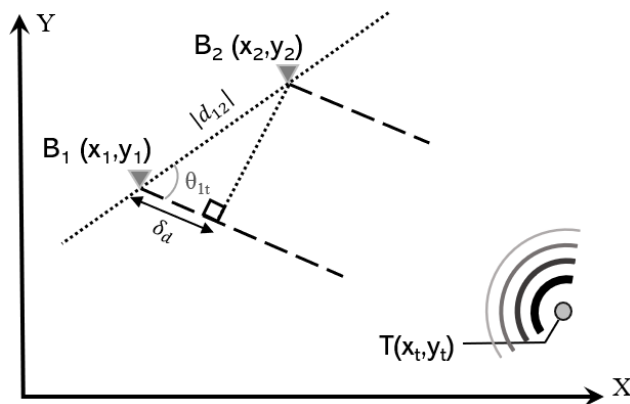


Figure 1.7. AoA measurements principle configuration. The AoA is measured with respect to the beacons-line intersection.

cons is measured, and apply the equation (1.10), the distance  $\delta_d$  can be calculated.

Typically the US, RF or Infrared (IR) signal are considered. For the received signal, the *far field* region is assumed [38, 39]. The far field condition guarantees that the received signal is a planar wave. In this way, the distance  $\delta_d$  can be related to the phase difference of the two received signal [40]:

$$\delta_d = \frac{\lambda \cdot \delta\phi}{2\pi} \quad (1.16)$$

Where  $\lambda$  is the wavelength, and  $\delta\phi$  the phase difference of the received signal.

- **Signal analysis.** The most important signal analysis technique is the RSSI. The RSSI measure the distance between the beacons and the target, correlating the signal power measurements with the distance.

The RSSI measures are relatively cheap and simple to implement in hardware. However, this approach requires detailed propagation models at RF, taking into account the variations in sensitivity and orientation of the receiver. Also, the propagation model changes depending on whether the application environment (indoor or outdoor) is, with obstacles or not. The transmitter node (beacon or

target, depend on the configuration) sends a signal with a certain power, which is reduced with the signal propagates. The greater is the distance from the receiver node, the lower is the strength of the signal that will reach this node according to the following equation:

$$P_r = \frac{P_t}{d^k} \quad (1.17)$$

Where  $P_t$  is the transmitted power,  $P_r$  the received power, and  $k$  the transmission factor whose value depends on the propagation environment [41]. In literature there are several models used to express the received power like: the *Friis model*, the *Log Normal model*, the *ITU-R model* and the, *Motrley-Keenan*.

- The Friis model is a relation based on a power balancing equation. Consider a wireless connection with a carrier frequency  $fc$  between the transmitting antenna and the receiver antenna at distance  $d$ . Assume low directive antennas (for the receiver and transmitter) in LOS condition in a free space, the distance  $d$  is related to the transmitted power  $P_t$ , and the received power  $P_r$  with a simple energy balance:

$$P_r(d) = P_t \frac{G_t A_r}{L_t 4\pi d^2} \quad (1.18)$$

Where  $G_t$  is the gain of the transmitting antenna,  $L_t$  indicates the loss factor on the transmitter, and  $A_r$  is the effective area of the receiving antenna [42].

In case of propagation with reflections, there are multiple paths propagation. The Friis formula is completed by one component that also considers the reflected power (Two-Ray Model).

- Log Normal model. For channels in NLOS, the presence of the multipath phenomena propagation, fading and shadowing, makes much more complicated to identify the exact patterns for path loss. It occurs experimentally that the received power decreases with distance more quickly than in free space. In this case, the relationship between the receiver power and the

distance, is represented by the following log-normal model:

$$P_r(d) = P_0(0) - n \, 10 \log_{10} \left( \frac{d}{d_0} \right) + X_\sigma \quad (1.19)$$

Where  $P_0(0)$  express in [dBm] is the reference power measured at one reference distance  $d_0$  from the transmitter, and  $n$  is the path loss exponent. The terms  $n$  measures the rate at which the received power decreases with distance. It is assumed to be constant, but recent studies suggest that it is more accurate modelled with a Gaussian random variable or, the different path loss exponents must be used respectively in far field and near field condition.  $X_\sigma$  is a random Gaussian distribution variable of mean 0 and variance  $\sigma^2$  which takes into account the effect caused by shadowing. Both  $n$  and  $\sigma$  depend on the environment in which the measurement takes in place [43].

- The ITU-R model, is a model that calculates the attenuation of the transmitted power in an indoor environment, where the nodes are also arranged on different floors of the same structure. The attenuation is defined as follow:

$$PL = P_r - P_t = 20 \log(f) + n \log(d) + L_f(k) - 28 \quad (1.20)$$

Where  $f$  is the transmission frequency,  $n$  is the path loss coefficient,  $k$  is the number of floors between transmitter and receiver, and  $L_f(k)$  is the loss factor due to the penetration of the floors [44].

- The Motrley–Keenan model can be applied in indoor environments where the presence of communication obstacles takes place in NLOS. Attenuation assessed at the frequency of 2.4 GHz can be expressed as:

$$PL = P_r - P_t = 40 + n \log(d) + \sum_{m=1}^M P_m + \sum_{k=1}^K P_k \quad (1.21)$$

Where  $P_m$  is the attenuation related to the  $m$  walls and  $P_k$  to the  $k$  floor with respect to the transmitter and receiver [45].

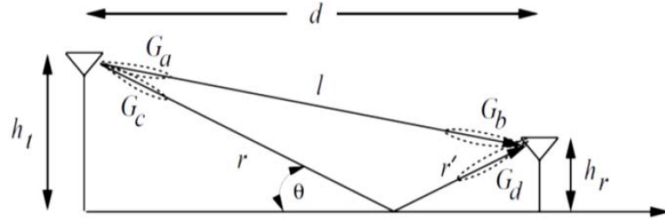


Figure 1.8. Two ray model path schematization [2].

The estimated distance is:

$$\hat{d} = d_0 \left( \frac{P_r}{P_0(d_0)} \right)^{-\frac{1}{n}} \quad (1.22)$$

The main advantage of use of the RSSI is the no need to additional hardware to perform the received power measurement, since the measurement algorithm is present by default in different technologies. The disadvantage is related to the fact that the measure come from a physical level, so the original signal is not examined but the signal version is affected by noise and interference, making the measurement very inaccurate.

## 1.2 Localization technologies and application

The main technologies involved for the localization problem are: *radio-frequency*, *ultrasonic*, and *infrared*. The technology of an IPS perform a heavy impact on the accuracy of localization, latency, scale and scalability, power consumption, and costs. In this subsection, the main aspect of those technologies and some IPS are analyzed.

### 1.2.1 Radio frequency

For the RF technologies, one or more properties of the electromagnetic wave radiated by a transmitter and received by a mobile station, were used for the target localization (e.g RSSI).

RSSI used as either a radio fingerprint or path loss power, achieve sub-meter-level localization accuracy in simple environments, because it

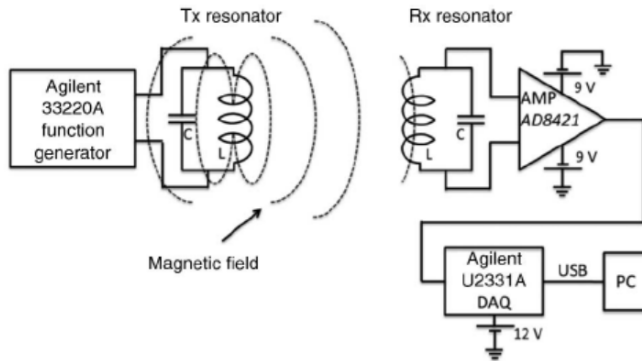


Figure 1.9. Indoor positioning system, based on two low-frequency coupled resonant antennas and the trilateration algorithm: the received and transmitted loop antenna are schematics with equivalent LC circuit [3].

suffers from dramatic performance degradation due to multipath, environmental variation and interfering sources; as other communication systems transmitting on the same bandwidth [46]. In [2], the algorithm Frequency Diversity (FD) was used with the ZigBee protocol, to improve the RSSI measurement, with a two ray-model to estimate the final distance. The two-ray model describes signal propagation when there is a direct and a reflected path between the transmitter and the receiver as showed in Fig.1.8 [47]. In the FD method, the transmitter sends the same message using different frequency channels, the receiver collects the different measure of RSSI at diverse frequency and applies simple algorithms to extract the RSSI value. The Authors compared three algorithms: Geometric Mean, Arithmetic Mean, and the Least Square Optimization, which achieved best results.

In [3], an indoor positioning system, based on two low-frequency coupled resonant antennas and a trilateration algorithm, was presented. The path-loss model relates the induced voltage on receiving loop antenna to a distance. The transmitter resonator was connected to the output of the Agilent 33220A function generator, providing a 24.4 kHz sinusoidal signal. An instrumentation amplifier, the AD8421 by Analog Devices, with a voltage gain of 100, was used to condition the loop antenna inducted voltage, and a data acquisition system, the U2331A by Agilent, was used to transfer the data to a PC for processing purposes (Fig.1.9).



Figure 1.10. The RFID reader and tag used in LANDMARC IPS [4]

The proposed system has a maximum error of 30 cm in a 14.0 m x 12.0 m area.

An important project for the RSSI localization techniques is the LANDMARC [4] (Fig.1.10). The localization system uses the RFID technology for the localization of the objects inside a building. Usually the RFID localization system use an anchor RFID reader node and a RFID tag to localize the target. In order to improve the accuracy more readers should be used, but they are more expensive than tag. In the LANDMARC approach also cheaper passive reference tags were used as anchor. The signal intensity of the reference tags is used to calibrate the uncertainty of the distance for tracking tags.

The distance calibration is performed by weighing summation of the  $k$ -nearest reference tags location. By utilizing the reference tags, LANDMARC can provide more accuracy with few Readers. LANDMARC deploys active tags as reference tags since they can provide information about the signal strength to detect the range of the tracking tag. This method benefits in reducing a large number of expensive readers by using extra cheap tags instead.

The RSSI measurement can be used to determine a radio tomographic imaging (RTI), in order to find the tag position. This technology applies an imaging approach onto active sensor nodes around a certain area. While a person is moving in this area, the received signal strength values of the single radio links are influenced and give information about the user's location and movement user. The most advantages of this techniques is the device-free user localization.

In [1], the Authors extract the RTI using a passive RSSI. The system uses a passive RSSI transponder (pRFID), mounted on the floor of a room and powered over the electromagnetic communication signals

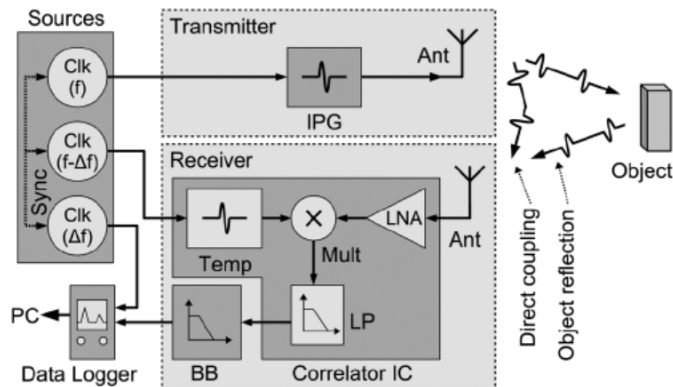


Figure 1.11. Block diagram of UWB movement detection system [5].

transmitted by a few reader antennas in the room edges. The difference between the transmitted and received signal power was used as physical measurement basis for human localization algorithms. The maximum error is 45 cm in a  $5\text{m} \times 5\text{m}$  area with three people localized.

Better performance can be achieved if an ultra-wide-band (UWB) impulse-radio is used. According to the definition of the U.S. Federal Communications Commission, the UWB is a short radio pulse, where any wireless transmission scheme occupies a bandwidth of more than 25% of a centre frequency or the absolute bandwidth larger than 500 MHz [48]. In [49], a hybrid system (RSSI-UWB) was presented. The RSSI measurements was used for estimating the coarse position, and the UWB radio is employed for fine position estimates, where centimeter-level accuracy is needed. In particular, a 10-cm accuracy is achieved in a  $3.0\text{ m} \times 5.0\text{ m}$  area. The UWB transmitter on the tag sends UWB pulses to the UWB readers. The readers measures the TDoA in order to compute the position.

In [5], a UWB movement detection system, based on sweeping impulse correlation, was presented (Fig.1.11). The impulse generator provides a continuous UWB impulse train at repetition rate  $f$ . The receiver receives first the direct coupling impulse and after the reflected impulse from the objects. The reflected impulse arrives after the direct impulse because the objects-antenna distance is bigger than receiver and transmitter antenna distance. The receiver first amplifies the received signal by a low-noise amplifier (LNA), and further processes it by a correlator

integrated circuit (Correlator-IC), in order to compute the correlation to the template impulse, and the LNA output signal.

The template impulse is generated with a  $(f-\Delta f)$  repetition rate, thus the template impulse is continuously sweeping with respect to the received impulse train. This implies two peaks on the correlator output corresponding to the direct coupling pulse and the reflected signal. The time distance of two peaks is related to the objects distance.

### 1.2.2 Infrared

The infrared light is an electromagnetic radiation with wavelengths of visible light, extending from the nominal red edge of the visible spectrum at  $700\text{ nm}$  to  $1\text{ mm}$ . This range of wavelengths corresponds to a frequency range of approximately  $430\text{ THz}$  down to  $300\text{ GHz}$ . The IPS based on IR signals, uses infrared signals in order to transmit signals from sensor nodes (or tag) to the beacon node. One of the most well-known infrared positioning systems is the active badges developed by AT&T Cambridge [50].

In this system, users carry an ID card equipped with infrared LED. The infrared LED sends a unique code every 15 s. Furthermore, there are infrared sensors installed on a ceiling and if the IR badge is within 6 m, the sensor is able to read the code. The beacon node receives the data from the IR sensors periodically. Finally, the anchor node is able to build a map of each badge location using the information retrieved from the sensors.

In [51], the Authors propose an optical wireless IPS using light emitting diodes (LEDs) and tested it via simulation. The positioning system technique is based on TDoA method. To estimate the locations of an object in the room, three LED lamps are used, each one with a unique frequency address (F-ID). Based on the property that LED can modulate signals while being used as a lighting device, each LED lamp transmits its assigned F-ID. The receiver detects phase difference between the transmitted signals, whereby time difference of arrival is estimated [52]. The Author evaluated the proposed method using computer simulation; the dimension of the system model is  $5.0\text{ m} \times 5.0\text{ m} \times 3.0\text{ m}$ . The maximum and mean values of location uncertainty during simulation were 4.5 mm and 1.8 mm, respectively.

The IR solution is a promising indoor positioning systems, specially in application where the use of RF are limited, such as: hospitals, air-



Figure 1.12. The 2016 HTC Vive beacon laser-scan and the headset.

planes, and areas with RF sensitive equipment.

An important IR IPS is the lighthouse tracking system of the HTC Vive headset, and the Minnesota scanner [53]. In Fig.1.12 the HTC Vive hardware is showed. first, the beacon laser scan emits a synchronization IR flash and after, sweeps an IR beam in the vertical and horizontal direction separately. On the headset a constellation of photodiodes is placed and, the constellation geometry is known. The detector IR matrix, detects the synchronization flash signal and the TDoA of the laser scan passage.

The rotation rate of the spinning drums is known and is analogous. The precise timing is recorded as the beam hits each photodiode. Considering the timing information the AoA is easily determined and then the orientation and position, with respect to the beacon laser station [54]. Multiple base stations can be used as well, in a way that is comparable to multiple cameras or multiple eyes to infer depth. The result is accurate tracking over a large area [55].

### 1.2.3 Ultrasonic

Ultrasound can be defined as acoustic waves with frequencies in the region of the acoustic spectrum that is not accessible to human perception. The human acoustic spectrum frequencies is from  $20Hz$  to  $20kHz$ , although, with age, the upper limit is significantly reduced [56]. This band of frequencies is only a tiny slice of the total available spectrum, the ultrasonic wave. Ultrasonics is defined as that band above  $20kHz$ . It continues up into the  $MHz$  range and finally, at around  $1GHz$ , goes over into what is conventionally called the hypersonic regime [39].

The most common technique used in ultrasonic localization are ToF

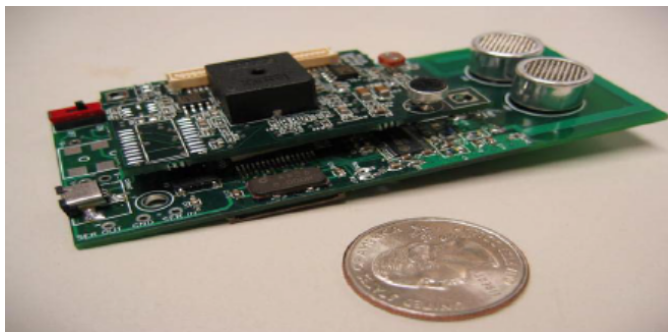


Figure 1.13. Cricket unit with sensor-board, working as either a beacon or a listener [6].

[57] and TDoA.

In [6], an important ultrasonic positioning system developed by the MIT Laboratories, the Cricket, is shown. The Cricket system consists of a small hardware platform formed by RF transceiver nodes (Cricket nodes), a microcontroller, and other associated hardware for generating and receiving ultrasonic signals (Fig.1.13). There are two types of Cricket nodes: beacons and listeners. Beacons periodically transmit an RF message containing specific information, such as a unique identifier, and the coordinates. Only the listeners within proper radio range can receive the information sent by beacon.

Each beacon transmits an ultrasonic pulse and at the same time the RF message. Listeners, with LOS connectivity to the beacon and within the ultrasonic range, will receive the RF message and the ultrasonic pulse. Because RF travels about  $10^6$  times faster than ultrasound, the listener can use the time difference of arrival between the start of the RF message from the beacon and the corresponding ultrasonic pulse, to calculate its distance from the beacon.

Like Cricket, DOPLHIN (Distributed Object Locating System for Physical-space Internetworking) [58] uses ultrasonic sensor node to localize a target. Each node is made by two ultrasonic transducers: one for transmitting and another for receiving. The system can be configured in two ways: *centralized*, and *privacy-oriented*.

In *centralized* mode, the mobile node works as a transmitter and the others nodes as receivers, with a central node that calculates the mobile position based on ToF measurements returned by the receiver nodes.

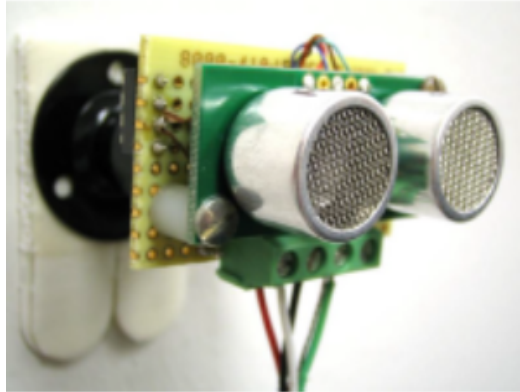


Figure 1.14. Devantech wall-mounted ultrasonic sensor. Two separate ultrasonic sensors were used, one for transmitting the ultrasonic burst and another for receiving the corresponding echo [7].

In *privacy-oriented*, the mobile node works as a receiver, and calculates its own position. With respect to the Cricket, for the DOLPHIN, the location of objects is automatically determined in a distributed manner using only few manually configured references.

In [7], a tag-free 2D positioning was discussed. The system uses a low cost Devantech ultrasonic sonar-module mounted on the wall room (Fig.1.14). Two types of sonar module are used: *active unit* and *passive unit*. The *active unit* is composed by a sonar-module that emits an ultrasonic signal and records the primary echo from the localization objects. The *passive units* receives direct path, echoes and reflections from target signal originating from the *active unit*. The return signals are highly variable in time due to noise, inherent multipath and non stationary reflections causing constructive and destructive interference. Thereby, several signal processing steps are necessary to determine the distances measures: time-average techniques to remove the presence of static objects, and state the strong echo and then a clustering to estimate the several distances candidate. Finally, the tracking algorithm determines the 2D position using the clustering processing results. The prototype is tested in a  $6.0\text{ m} \times 5.0\text{ m}$  area, using one *active module* and six *passive module*. The maximum error is 0.51 m with a 10 s maximum time algorithm convergence.

In [8], the TDoA method is used to determine a human 3D position in

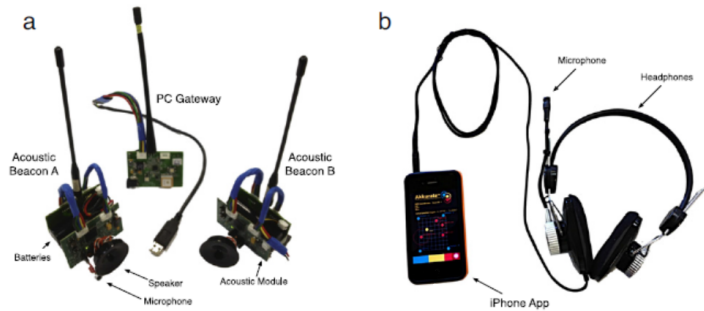


Figure 1.15. System devices: (a) Acoustic Beacons and Gateway, (b) Mobile Device based on a iPhone 4S [8].

a room. The Authors propose a system composed by four acoustic beacons, one microphone mounted on the top of headphone, and a iPhone connected to the microphone (Fig.1.15). The smart-phone computes the position using the proposed positioning application (Akkurate). The acoustic beacons use a System-on-Chip (SoC) with a built-in low-power RF transceiver and a piezo-tweeter for transmitter the US signal. The RF transceiver is used for both communication and synchronization. The Authors proposed Automatic Time Synchronization and Syntonization protocol that achieves a clock offset error of less than  $5 \mu\text{s}$ . Acoustic beacons are programmed to periodically transmit a chirp pulses while the mobile device measures the TDoA of received signal whit a correlation and a decimated energy estimator. The proposed system offers an absolute error of less than 10 cm for a position refresh period of 350 ms.

The drawbacks of US solution are the occlusion problem and the limited cover area; the main advantages are the low-cost transceivers and low power consumption.

#### 1.2.4 Other

Other technologies are available for the IPS, like the *camera based solution*. The fundamental use of this approach is based on image cues extraction and comparison of consecutive frames. In general, cues used for object tracking are color, motion, orientation, spatial energy, shape, texture, depth, disparity, etc. The cues are obtained by using a sensor, Single-Modal (SM), or different sensor Multi-Modal (MM).

In single modal only vision or thermal camera are used. In multi-

modal the camera system is combined with IR system, RFID and other technologies.

In [59], the Authors proposes a probabilistic method to solve the occlusion problem presented in deterministic methods. Cue reliability in current frame, was based upon its performance in previous frames, and overall probability map was estimated as weighted sum of individual maps, while; the tracking is based on the previous tracking results.

In [60], a tracking object algorithm in an urban scenery was proposed. The Authors propose a novel multi-scale object extraction procedure with two-stage segmentation approach. First, a coarse supervised segmentation removes the non-object regions corresponding to known background categories such as road, building or vegetation. The second stage performs a fine unsupervised multi-scale segmentation to extract scale-stable object proposals from the remaining scene regions. In particular, the algorithm can be exploited also in indoor environments due to the fact that a urban scenery was used. The test is performed on stereo-vision KITTI [61] data set in numerous scenarios.

In [62], a multi-modal tracking system based on vision camera and a RF radar was presented. In this work, the radar gave low resolution bearing information, and was compensated by vision camera for multiple object tracking.

Another example of multi-modal system is discussed in [63]: the Author combined a IR emitter LED with a stereo camera, and the tag is provided with a infrared red emitter. To achieve multi target detection, each tag emitter had a unique identification code. The stereo camera detects the IR radiation, and thanks to a calibrate camera model, the target. The camera based solution required an expensive hardware in order to achieve a high accuracy and a faster target localization, but the localization method is not so invasive.

### 1.3 Positioning tracking system for surgery application

Thanks to the innovation in the localization technologies, even in the medical field the IPS becomes essential. The main application regards the surgery instrument tracking in the operating room and the training phase based on augmented reality [64]. The main features affecting the tracking systems are certainly latency ( $< 30\ ms$ ) and accuracy ( $< 5\ mm$ )

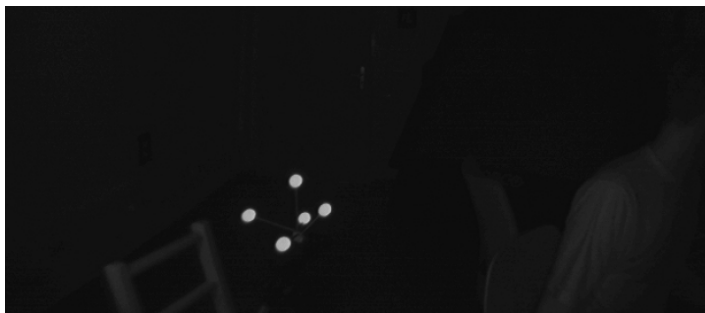


Figure 1.16. Example of reflectors markers visualization in the IR spectrum.

[65]. There are numerous tracking devices on the market for medical uses, based on electromagnetic sensors or infrared optical cameras (Optotrak, NDI) [66]. The main common technologies are the *Optical tracker* and the *magnetic tracker*.

### 1.3.1 Optical Tracker

Optical trackers are currently the most popular in surgical applications and are hardly influenced by clinical environments, ensuring precision of millimeter measurement [67]. Optical tracking systems consist of infrared stereo cameras synchronized with an infrared emitter and optical reflectors markers (Fig-1.16). The cameras are used as reference nodes (beacons) while the markers are illuminated by the emitter system, so that they can be located in space. It is easy to understand that the number of targets that can be located is limited to the ability to discriminate markers associated with different objects and to the computing capacity necessary for extracting positions and orientation. In this type of system, cameras localize the markers.

The performance is strongly influenced by occlusions typically caused by the considerable number of instruments and personnel present during surgery. It should also be noted that optical trackers allow to obtain high performance in terms of accuracy and precision in the tracking of relatively large objects (a few centimeters), which is a disadvantage considering the tendency to reduce the size of surgical instruments.

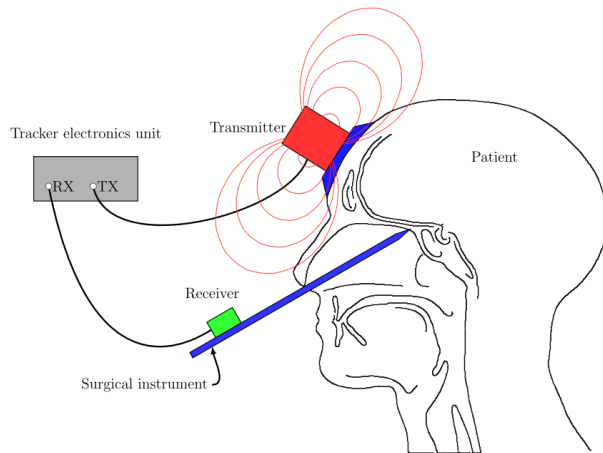


Figure 1.17. Electromagnetic tracking setup for surgical navigation. A head-mounted transmitter allows to control an instrument during sinus surgery [9]

### 1.3.2 Magnetic Tracker

The electromagnetic tracking systems are based on the principle of mutual induction or by the use of magnetic field sensors (magnetometers). The field generator produces a known electromagnetic field used to place small sensors located within the volume of interest. Trackers are gaining popularity due to their small size and easy integration [68, 69]. Magnetic location systems are made up of a field emitter which consist of permanent magnets or particular generators of variable electromagnetic field and magnetic detectors (Fig. 1.17 [9]). In the case of variable electromagnetic field generators, the sensors used transduce the received field into a potential difference related to the sensor-emitter distance. Using multiple sensors and the voltage measurement, it is possible to track the position and orientation of the object [70].

The main limitations of magnetic tracking are the magnetic distortion caused by the metal instruments and equipment present in the vicinity of the surgeon and the degradation of performance in work areas with volumes bigger than one square meter.

Technologies that are not affected by these types of problems are for example, the ultrasound. They are immune to the electromagnetic disturbances and their main problems are related to the presence of multi-

path and occlusions.

## Chapter 2

# Proposed Method

### 2.1 Conventional heading measurements System

Thanks to the recent improvements in Micro Electro-Mechanical Systems (MEMS) technologies, the application of inertial techniques in the indoor tracking field became more common and cheaper. A small chip combine easily 3-axis *gyroscope*, *accelerometer*, and 3-axis *magnetometer* all in the same package, referred to as IMUs. This has resulted in an increased interest in the topic of the inertial navigation.

It is a technique where measurements provided by accelerometer and gyroscope are used to track the position and orientation of an object. By processing the signals from the IMUs devices, it is possible to track the position and orientation. The position can be found if the velocity, while orientation and position are known at the starting point[71].

- **Gyroscopes.** The gyroscope is a sensor used to measure the rotation rate of a body. Theoretically, starting from the initial conditions, the gyroscope is sufficient for the rotation estimation by the integration of angular velocity. Unfortunately, a constant bias is present for the MEMS sensors even when the gyroscope is not undergoing any rotation. Integrated this error, an angular error which grows linearly with time, is present [72]. Additionally, an offset drift occurs over time, caused collectively by sensor axis misalignment, cross-axis sensitivities and even temperature effects. For instance, assuming a linear calibration model for the gyroscope:

$$\omega_{gyro} = a + b \omega_{true} \quad (2.1)$$

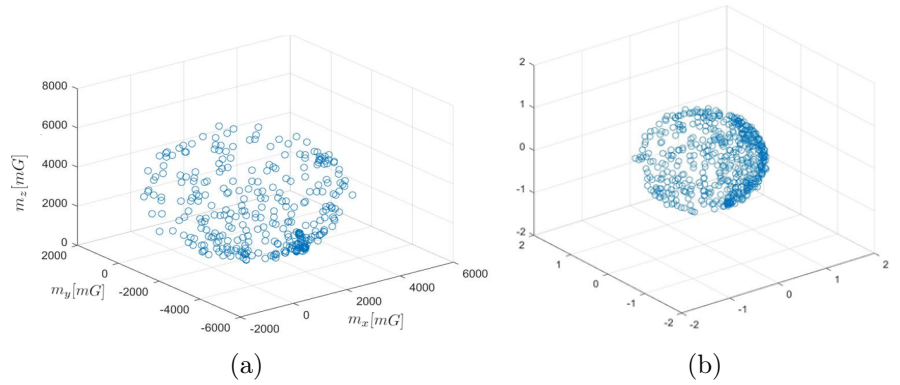


Figure 2.1. (a) Raw magnetometer measurements values for the 3-axis, noting the bias and eccentricities presence in the measurements. (b) Calibrated and normalized magnetometer value.

Where  $a = 0$ ,  $b = 1$  for an ideal gyroscope. The estimated angle error for one axis can be defined as the difference between the measured and the true angle:

$$\epsilon(t) = \alpha_{gyro}(t) - \alpha_{true}(t) = \int_0^t \omega_{gyro} dt - \int_0^t \omega_{true} dt \quad (2.2)$$

Even if no rotation was assumed  $\omega_{true} = 0; \forall t \geq 0$  the error grows linearly over time:

$$\epsilon(t) = at \quad (2.3)$$

Fusion algorithms with other sensors (e.g. accelerometer) could estimate this drift and correct it in real-time.

- **Accelerometer**, The accelerometer is a device that measures constant accelerations like the force of gravity as well as dynamic accelerations by moving the accelerometer. Typically, the MEMS sensors give us very accurate measurements if a calibration is applied. The calibration is needed to remove systematic measurement bias, which vary in temperature and in time.
- **Magnetometer**. The magnetometer is a device that measures the strength and direction of the magnetic field. The typical use of magnetometer is to provide information about the vector pointing

of the true North, measuring the earth magnetic field.

In indoor navigation, the measurements of the local magnetic field, result by the sum of multiple magnetic fields. The magnetic field is present on the local frame of the sensor plus the Earth's magnetic field. The unwanted or interfering magnetic fields can be classified into two distinct groups: hard-iron and soft-iron interference's effect[73].

The first group consists of constant or slow time-varying fields generated by ferromagnetic structural materials near the magnetometers (hard-iron). The hard-iron offset is a vector which adds up to the magnetometer reading.

The second group of interfering magnetic fields result from materials that generate their own magnetic field in response to an externally applied field.

Both generated fields are affected by the magnitude and direction of the externally applied magnetic field (e.g. the presence of big metal mass). Such materials are called soft irons and the error they generate is referred to as a soft iron bias.

Magnetometer calibration methods take into account offsets because of hard-iron bias and eccentricities because of soft-iron bias (Fig.2.1a, 2.1b). It is possible to relate the hard iron distortions with the device, while the soft iron distortions within the environment where the device is located. Calibration methods mitigate these effects, but they fail with the presence of non-uniform magnetic disturbance [74, 75, 76].

In most applications, the sensitive 3-axes of the sensors coincide with the axes of the orthogonal frame in which the sensors are mounted. The *roll* is a counterclockwise rotation of  $\gamma$  about the z-axis. The *pitch* is a counterclockwise rotation of  $\beta$  about the x-axis. The *yaw* is a counterclockwise rotation of  $\alpha$  about the y-axis (Fig.2.2).

Apply sensor fusion algorithms to the gyroscope and accelerometer measurements, the pitch and roll estimation are possible [77]. Gyroscope allows to assess the dynamic orientation by measuring and integrating angular velocity.

The principle operation for the orientation and position estimation based on IMU measurement, is summarized in the Fig.2.3, without the

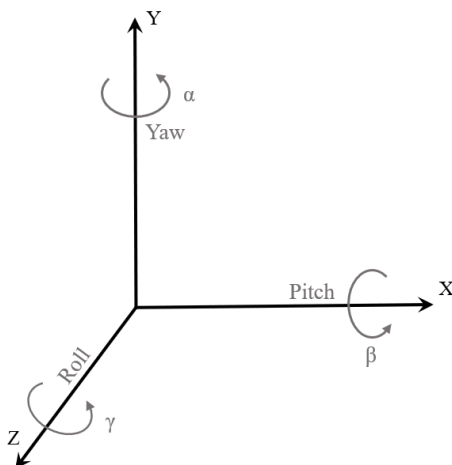


Figure 2.2. Pitch, roll, and yaw representation.

drift compensation. Accelerometer allows us to assess the static orientation by measuring the projection of the gravity vector acceleration, and the dynamic accelerations. The accelerometer compensate the pitch and roll drift due to the gyroscope. Ideally, also the yaw angle can be estimated using the gyroscope but, due to the drift, a divergent yaw estimation is present over time. However, the angular velocity integration causes a divergent orientation error, both in static and dynamic conditions, even with drift compensation [71, 72]. The magnetometer measurements are necessary for the yaw angle estimation and give a contribute for the dynamic assessment of the all angles [78, 79, 80, 81]. As previously discussed, the magnetometer correction fails in presence of magnetic disturbance, for this reason an ultrasonic heading (yaw) measurements system was developed.

## 2.2 The Ultrasonic heading System

In subsection 1.2.3 an overview on the US based localization system is presented. The key idea is to use the US signal in order to computing the heading of a target. The ultrasonic heading measurements can be used for the yaw angle compensation in a magnetometer-less IMU. The principal components of the proposed ultrasonic heading system (UHS) are an US emitter and two ultrasonic sensor receiver (USr).

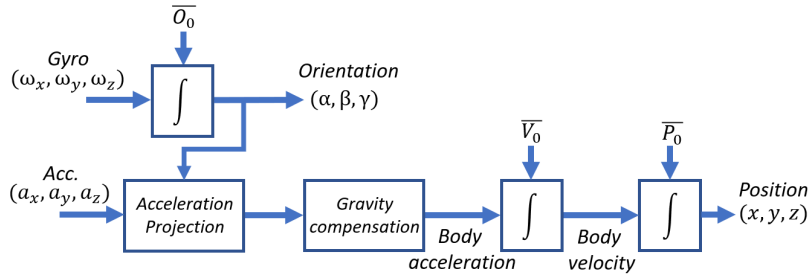


Figure 2.3. The initial condition for orientation, velocity and position indicated respectively with  $\overline{O}_0$ ,  $\overline{V}_0$ ,  $\overline{P}_0$ . The orientation information, combined with the acceleration measurements, are needed to compute the true Body acceleration.

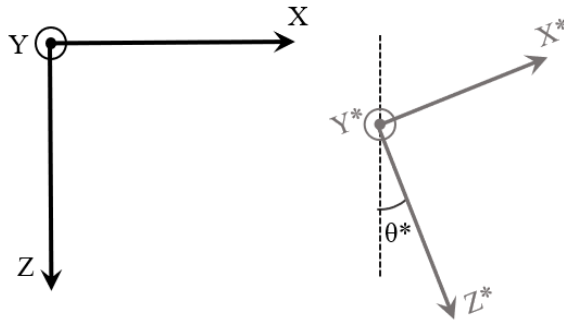


Figure 2.4. The angle  $\theta^*$  is the positive heading (yaw) angle of the localized frame  $(X^*, Z^*)$  with respect to the reference frame  $(X, Z)$ .

### 2.2.1 Measuring principle

Assuming the geometrically configuration in Fig-2.4, the heading can be defined as the mutual orientation between the reference frame (FR) and the localized frame (LF), considering the same pitch and roll.

The  $(X, Z)$  is the FR, the angle  $\theta^*$  is the LF heading. The US wave is generated by the FR to the LF frame. The received signal is assumed plane wave (far-field assumption). Thanks to the far field condition, the US signal received by the two USr is a plane wave perpendicular to the propagation direction  $\vec{r}$ . For instance, the far Fidel condition is verified

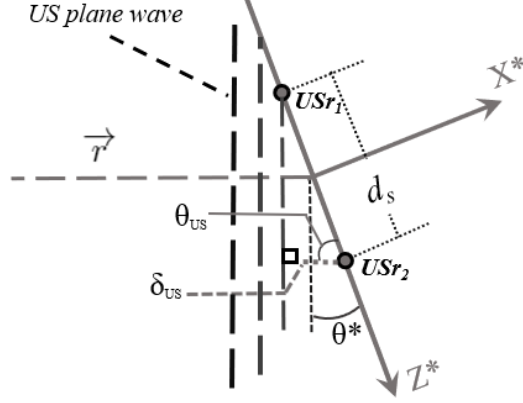


Figure 2.5. The received plane wave signal. The heading angle  $\theta^*$  is related to the  $\delta_{us}$  distance measurements.

for a circular aperture at the distance:

$$|\vec{r}| > \frac{D^2}{4\lambda} \quad (2.4)$$

where  $D$  is the aperture of the US emitter and  $\lambda$  the US wavelength [39].

In Fig.2.5 the geometrical problem of the heading estimation is sketched. The propagation direction  $\vec{r}$  and the US received plane wave were reported. Similar to the AoA estimation (subsection 1.1.2, the angle  $\theta_{us}$  is equal to:

$$\theta_{US} = \arccos\left(\frac{\delta_{US}}{d_s}\right) \quad (2.5)$$

The term  $d_s$  is the USr known distance, the term  $\delta_{us}$  is the difference for the US plane wave path toward the two USr:

$$\delta_{US} = c \delta_t \quad (2.6)$$

Where  $c$  is the sound speed and  $\delta_t$  the TDoA of the US plane wave received to the two USr.

The geometrical problem of the frame orientation measurement is solved in time domain. Assuming a plane wave received sinusoidal, the distance  $\delta_{US}$  can be related to the phase difference of the two received

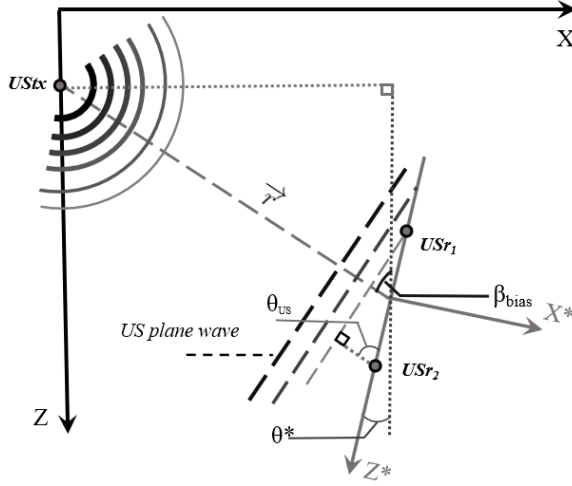


Figure 2.6. Generic angle projection. The  $\beta_{bias}$  correction term depends on the US relative emitter-LF position.

signal [40]:

$$\delta_{US} = \frac{\lambda \delta\phi}{2\pi}, \text{ with } \delta_{US} < \frac{\lambda}{2} \quad (2.7)$$

Where  $\lambda$  is the US signal wavelength and  $\delta\phi$  the phase difference. The condition  $\delta_{US} < \frac{\lambda}{2}$  in the eq.(2.7) solves the ambiguity phase problem, and can be guaranteed if  $d_s < \frac{\lambda}{2}$  (Fig.2.5) [82].

According to the Fig.2.5 schematization, the heading angle  $\theta^*$  is equal to:

$$\theta^* = \frac{\pi}{2} - \arccos\left(\frac{\delta_{US}}{d_s}\right) \quad (2.8)$$

The equation (2.8) returns the heading angle defined in Fig.2.4 if the US propagation direction  $\vec{r}$  is orthogonal to the  $Z$  axis of the FR.

In Fig.2.6 the generic case study is sketched. A bias angle  $\beta_{bias}$  is present in the measurements if the  $\vec{r}$  is not orthogonal to the  $Z$  direction. For instance, assuming  $\theta^* = 0 \text{ deg}$  in Fig.2.6, the  $\theta_{us}$  angle is not zero and less than  $\frac{\pi}{2}$  and, causes wrong estimation if the eq.(2.8) is considered. For this reason, the bias terms  $\beta_{bias}$  must be considered for the heading estimation. The generic heading is equal to:

$$\theta^* = \beta_{bias} - \arccos\left(\frac{\delta_{US}}{d_s}\right) \quad (2.9)$$

Assuming the LF origin position  $(X_*, Z_*)$  with respect to FR and the US emitter in the position  $(0, Z_{tx})$ , the bias terms is equal to:

$$\beta_{bias} = \arccos\left(\frac{Z_* - Z_{tx}}{|\vec{r}|}\right) \quad (2.10)$$

The distance  $|\vec{r}|$  is greater than zero according to the far field assumption eq. (2.4).

The  $\beta_{bias}$  terms is linked to the position of the LF. The eq.(2.8) is got from the eq.(2.10) when  $Z_* = Z_{tx}$ .

### 2.2.2 Sine-Fit based phase difference extraction algorithm

The  $\delta_\Phi$  from the eq. (2.7) is usually computed by measuring the time interval between US signal arrival at USr1-2. The TDoA can be measured through the zero crossing detection algorithm [82]. In case of noise, the zero crossing detecting of the US signal is misleading [83].

The standard sine fitting algorithm is applied in order to extract the phase from the received signal at USr1-2. Several authors exploited sine fit to assess distance [84], but only to compensate the phase-shift [85] or to estimate the components of distortion [86] or in asynchronous sampling [87].

Fitting consists in adjusting the parameters of the mathematical model in order to minimize the distance measurement between the model and the digitized signal. The three parameters sine fitting (3pSF) is aimed at accurately estimating the amplitude, phase and DC value of a sinusoidal signal corrupted by noise [84, 88]. The three parameters sine fitting (3pSF), is utilized when the signal frequency is known and stable.

Assuming a received sinusoidal signal, the signal model is:

$$y_k = A \cos(2\pi\nu k + \varphi) + DC + W_k, \quad \nu = \frac{f}{f_s} \quad (2.11)$$

Where  $f$  is the signal frequency,  $f_s$  the sample frequency,  $A$ ,  $\varphi$  and  $DC$ , respectively, the amplitude, phase and DC value,  $W_k$  the noise, and  $k$  the digital time ranging from 0 up to  $M - 1$ . The equation (2.11) can be arranged as follows:

$$y_k = A_0 \cos(2\pi\nu k + \varphi) + B_0 \sin(2\pi\nu k + \varphi) + C_0 + W_k \quad (2.12)$$

$$\text{where : } A_0 = A \cos \varphi, B_0 = -A \sin \varphi, C_0 = C \quad (2.13)$$

The eq.(2.12) is equivalent to the eq.(2.11), but linear in the parameters 2.13. Discarding the noise  $W_k$  and ranging  $k$  from 0 to  $M-1$ , eq.(2.12) it can be written in a linear system of  $M$  equations, represented in matrix form by [89]:

$$D \cdot x = y \quad (2.14)$$

Where  $x$  is a column array with the unknown components  $A_0, B_0$  and  $C_0$ ,  $y$  is a column array containing the samples of the input digital signal  $y_k$ , and  $D$  is the matrix of the coefficients:

$$D = \begin{bmatrix} C_{00} & S_{00} & 1 \\ \cdot & \cdot & \cdot \\ \cdot & \cdot & \cdot \\ C_{0k} & S_{0k} & 1 \\ \cdot & \cdot & \cdot \\ \cdot & \cdot & \cdot \\ C_{0M-1} & S_{0M-1} & 1 \end{bmatrix}$$

where the matrix elements are:

$$C_{0k} = \cos(2\pi\nu k), S_{0k} = \sin(2\pi\nu k) \quad (2.15)$$

The 3pSF algorithm determines  $x$  by means of the pseudo inverse method, namely:

$$x = (D^T \cdot D)^{-1} D^T Y \quad (2.16)$$

The solution represented by eq. (2.16) minimizes the mean square value of the residue of the fitting, which should coincide with the noise [33, 89]. The parameters of the model given in (2.11) are finally estimated through:

$$\begin{cases} A = \sqrt{A_0^2 + B_0^2} \\ \varphi = \arctan 2(A_0, B_0) \\ DC = C_0 \end{cases} \quad (2.17)$$

The  $\arctan 2(\dots)$  represents a four quadrant inverse tangent function [90]. Apply the 3pSF the phase, amplitude and the offset from the received signal at USr1-2 can be estimated. The two reconstructed sine

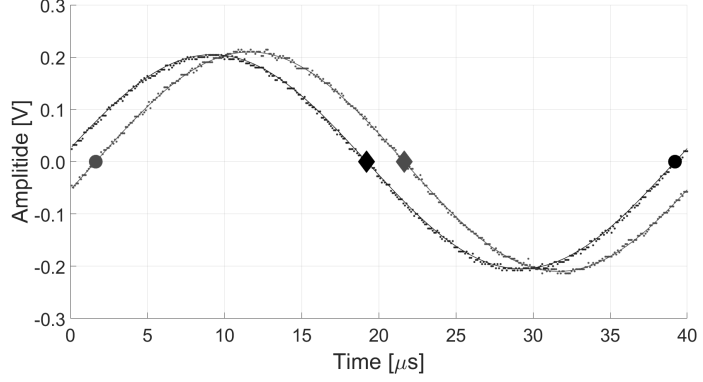


Figure 2.7. Time difference extraction for the same signal slope: (i) wrong (●), directly by eq. (2.19),  $\delta t_{phase} = -37.5 \mu s$ ; and (ii) correct (◆), by the proposed algorithm,  $\delta t_{algo} = 2.43 \mu s$ .

signals can be written as:

$$v_{chi}(t) = A_i \cos(2\pi f_s t + \varphi_i) + DC_i, \quad i = 1, 2 \quad (2.18)$$

Assuming  $v_{ch1}(t)$  as a reference, the relative phase shift represents the TDoA. In particular, the zero crossing time difference represent the terms  $\delta t$  in the eq. (2.6).

For a positive rotation (Fig.2.5), the  $v_{ch2}(t)$  is in late with respect to the  $v_{ch1}(t)$ , and vice versa for a negative rotation. Removing the  $DC$  component from the reconstructed signals, the zero crossing time difference can be obtained using the condition:  $v_{ch1}(t) = v_{ch2}(t) = 0$ . The instants satisfying the condition are:

$$t_1 = \frac{\frac{\pi}{2} - \varphi_1}{2\pi} T; \quad t_2 = \frac{\frac{\pi}{2} - \varphi_2}{2\pi} T \quad \rightarrow \quad \delta t = \frac{\varphi_2 - \varphi_1}{2\pi} T \quad (2.19)$$

where  $T$  is the period of the cosine signal.

According to the eq. (2.18), three zero crossing points can be intercepted. The times  $t_1$  and  $t_2$  in the eq. (2.19) represent one of the three possible zero crossing points. Each zero crossing point can be shifted by a quantity multiple of  $\pi$  in the phase domain, owing to the sine-fit algorithm's features. The phase shift can cause a  $\delta t$  wrong calculation, highlighted in the experimental example of Fig.2.7.

**Table 2.1** Time difference extraction.

---

```

1: function DELAY( $\varphi_1, \varphi_2$ ) ▷ Where  $\varphi_1$  and  $\varphi_2$  are the sine-fit phase output and  $\delta t$ 
   the time delay estimated
2:    $t_1 = \frac{\frac{\pi}{2} - \varphi_1}{2\pi} T$ 
3:   if  $t_1 < 0$  then
4:      $k = 1$ 
5:     while  $t_1 < 0$  do
6:        $t_1 = \frac{k\pi + \frac{\pi}{2} - \varphi_1}{2\pi} T$ 
7:        $k++$ 
8:     end while
9:   end if
10:   $t_2 = \frac{\frac{\pi}{2} - \varphi_2}{2\pi} T$ 
11:  if  $t_2 < 0$  then
12:     $k = 1$ 
13:    while  $t_2 < 0$  do
14:       $t_2 = \frac{k\pi + \frac{\pi}{2} - \varphi_2}{2\pi} T$ 
15:       $k++$ 
16:    end while
17:  end if
18:   $\cos'_{t_1} = -\sin(\frac{2\pi}{T}t_1 + \varphi_1)$ 
19:   $\cos'_{t_2} = -\sin(\frac{2\pi}{T}t_2 + \varphi_2)$ 
20:  if  $\cos'_{t_1} \cdot \cos'_{t_2} > 0$  then
21:     $\delta t = t_1 - t_2$ 
22:  else
23:    if  $t_1 < t_2$  then
24:       $t_1 = t_1 + \frac{T}{2}$ 
25:    else
26:       $t_2 = t_2 + \frac{T}{2}$ 
27:    end if
28:     $\delta t = t_1 - t_2$ 
29:  end if
30:  return  $\delta t$ 
31: end function

```

---

Assuming the condition in the eq.(2.7), the time difference extraction algorithm (TDeA) in Table 2.1 solves the  $\delta t$  wrong calculation. The condition (2.7) guarantees a maximum phase shifting of  $\delta\Phi < \pi$ . Then, the same sign of the first order derivative at the zero crossing point is obtained.

In the initial difference extraction phase (lines 2-17, Table 2.1), the TDeA found the first positive zero crossing times  $t_1$  and  $t_2$ , and compute the time difference assuming the  $vch1(t)$  as a reference. At line 20, the derivative sign is evaluated in order to find out the first times  $t_1$ ,  $t_2$ , where the reconstructed cosine function has the same slope. In this way, the proper  $\delta t$  is computed (Fig.2.7).

## 2.3 First prototype Ultrasonic IPS

In section 2.2.1, the US heading measurements principle is presented. The heading measurements is closely related to the positioning measurements. For this reason, a proof-of-principle demonstrator based on ultrasonic technology was realized.

The TDoA was measured by means of a microcontroller-based board Nucleo STM32L152RE, combined with a custom receiving circuit. The position was computed using a personal computer after the timing demonstrator acquisition, applying the TDoA technique [91]. Two different fixed US beacons were recognized and the time of arrival from the US receiver node, in order to computing the TDoA.

### 2.3.1 Beacon node recognition criteria

The different US beacons were recognized by comparing the received signal with a threshold: when the signal is greater than the threshold, a counter was incremented. If the signal is observed in a fixed time window, the counter value (NTH) depends only on the time shape of the received signal. The beacons were driven by a sinusoidal signal; thereby, if different signal frequencies were emitted by the beacons, the NTH counted at the receiver node was different. The observation time is less than the steady state sensor time; therefore, the received signal observed in the time windows isn't a sinusoidal but a damped sinusoidal signal [83], because the receiver and transmitter sensor are in a transient phase

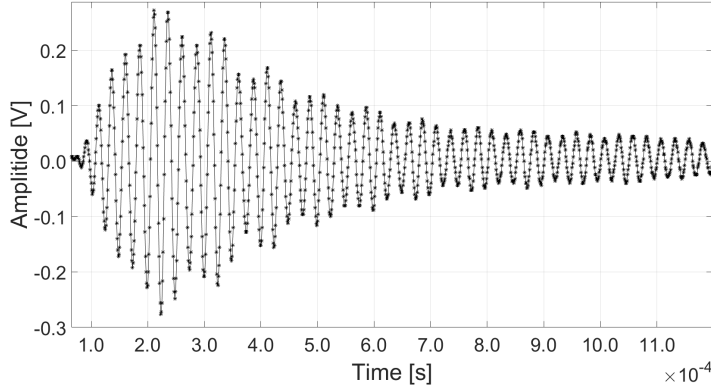


Figure 2.8. Real damped response of the *SensComp's Series 9000* ultrasonic sensors, stimulated by a  $f_4 = 40 \text{ kHz}$ ,  $10 \text{ Vpp}$  single burst signal (sample frequency  $f_s = 1 \text{ MHz}$ ).

(Fig.2.8).

$$v(t) = \left(\frac{t}{T}\right)^m \exp\left(\frac{-t}{T}\right) \cos(2\pi f_0 t + \phi) \quad (2.20)$$

For the proof-of-principle demonstrator, only two beacons were used, because the aim of this work is to demonstrate the recognition of different beacons in a low time (e.g.  $500 \mu\text{s}$ ). For this particular prototype set up, an observation time window of  $T_{ob} = 450 \mu\text{s}$  was required to recognize two or more beacons.

The time  $T_{ob}$  is composed by two terms: (i) the actual time  $T_{rg}$  spent to recognize the beacon and (ii) a damping time  $T_{dp}$  necessary to suppress the sensor oscillation.

The US beacons were driven in burst mode with sine waves at different frequency in a finite comparable  $T_{rg}$  time windows. The burst mode consists of sending, in a fixed time window, a certain number of sine waveforms using a burst of  $NT1_{TX} = 4$  and  $NT2_{TX} = 7$  for the frequency  $f_1 = 25 \text{ kHz}$  and  $f_2 = 50 \text{ kHz}$  sinusoidal signal, counting  $NTH_1 = 4$  for  $f_1$  and  $NTH_2 = 8$  for  $f_2$  at the receiver node. Also the frequency  $f_3 = 30 \text{ kHz}$  and  $f_4 = 40 \text{ kHz}$  can be used (Fig.2.20), in this case the receiver node counting respectively  $NTH_3 = 5$  and  $NTH_4 = 7$  with a sent burst value of  $NT3_{TX} = 5$  and  $NT4_{TX} = 6$ .

In general, the frequency was selected according to the US sensor frequency response and to the time  $T_{rg}$ . In this prototype, the *Sen-*

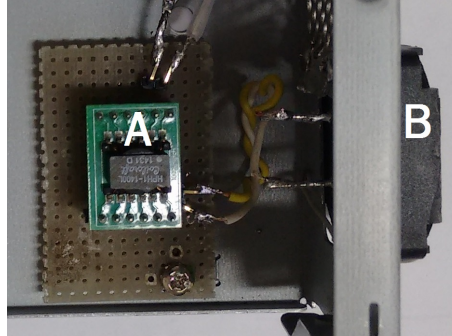


Figure 2.9. Transmitter beacon node: (A) the low-power signal coupling transformer, and (B) the ultrasonic sensor *SensComp's Series 9000*.

*sComp's Series 9000* ultrasonic sensors were used for the reference and receiver nodes, a minimum value of  $T_{ob} = 450 \mu s$  was obtained with a maximum of four distinct usable frequency values. At the beginning, the recognition time can be reduced if a high-speed sensor is available.

### 2.3.2 Transmitter node

The transmitter nodes are composed by the ultrasonic sensor *SensComp's Series 9000* and a signal transformer (Fig.2.9). To work properly in transmitting mode, the US sensor needs a high voltage input signal; thereby, the signal transformer was used to elevate the driving voltage generated by the Agilent 33220A function generator. The maximum peak-to-peak sinusoidal voltage available by the Agilent is 20 Vpp, hence a sine wave with 100 Vpp was reached by using a transformer with a ratio of 1:5.

The function generator was programmed in burst mode with external trigger; therefore, when an external trigger was received, a specific burst of sinusoidal function was generated at the output channel. For the twofold beacons at  $f_1 = 25 kHz$  and  $f_2 = 50 kHz$ , respectively four and eight burst-cycles were set up.

### 2.3.3 Receiver node

The main blocks of the receiver node are: the microcontroller Nucleo STM32L152RE, the ultrasonic sensor *SensComp's Series 9000* and a

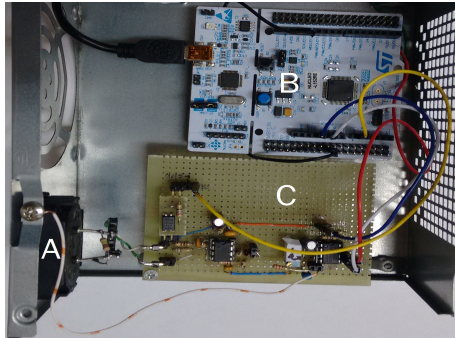


Figure 2.10. Receiver node: (A) the ultrasonic sensor *SensComp's Series 9000*, (B) the microcontroller Nucleo STM32 L152RE, and (C) the board custom circuit.

custom sensor-microcontroller interface circuits (Fig.2.10). The custom interface circuit includes three stages: damping circuit, analog amplifier stage, and a square circuit stage. The damping circuit was composed by a one-channel optoisolator, connected in parallel to the ultrasonic receiver. When the optoisolator was activated, the damping time was reduced thanks to the low resistance offered by the optoisolator that forces the sensor in the steady state. The analog amplifier stage was composed by a dual operational operational amplifier (OP) in single-supply mode, in order to amplify and filter the small-amplitude output signal arising from the receiver. The total gain of the two-stage amplifier is about 56 dB, with a  $f_l = 16 \text{ kHz}$  lower cutoff frequency, and a  $f_h = 100 \text{ kHz}$  upper cutoff frequency. The analog amplifier output was connected to the square circuit. The square circuit was composed by a hysteresis comparator with adjustable threshold voltage. The scope of the comparator circuit was to convert the threshold passage of the received signal in a pulse. Finally, the comparator output was connected to the microcontroller in order to count the number of threshold passages.

The microcontroller operation can be summarized as follows:

1. When a rising edge at the output of the square circuit was detected, two timers (*timer1*, *timer2*) were started, while a counter was enabled. *Timer1* was set to wait  $Trg = 150 \mu s$ .
2. During the time observation window  $Trg = 150 \mu s$ , the counter counted the NTH pulses and stored the results in order to recognize

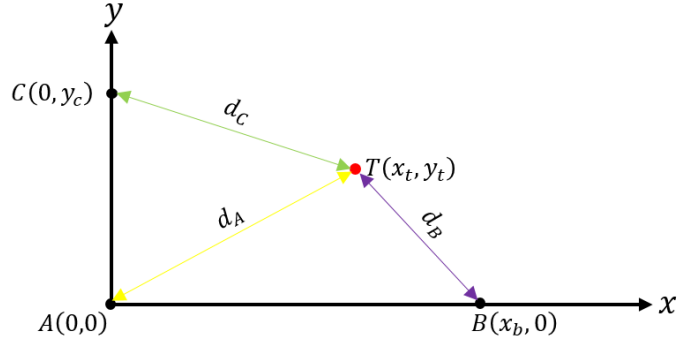


Figure 2.11. Geometrical 2D problem representation (A, B, and C: beacons; and T: target generic position).

the beacon.

3. After the time  $Trg$ , the counter was disabled, the damping circuit was enabled, and  $timer1$  was set to wait  $Tdp = 300 \mu s$ .
4. After  $Tdp = 300 \mu s$ , the counter was enabled, and the  $timer2$  was set to wait  $Trg = 150 \mu s$ .
5. When a rising edge was detected,  $timer2$  was read, and the procedure restarted from step 1), but without restarting  $timer2$ . The value of  $timer2$  represented the signal time arrival; thereby, the TDoA can be computed from the received signal as the difference between the starting value of  $timer2$  and the read value of  $timer2$  at the step 5).

In this way, the microcontroller could calculate the TDoA and recognize the sequence of signals coming from different beacons.

### 2.3.4 Localization algorithm

The localization algorithms implemented was the trilateration based on the TDoA. The localization performance was tested by means of a TDoA technique implemented in a Matlab<sup>®</sup> code. In Fig.2.11, the localization problem in 2D is sketched. The distance difference between

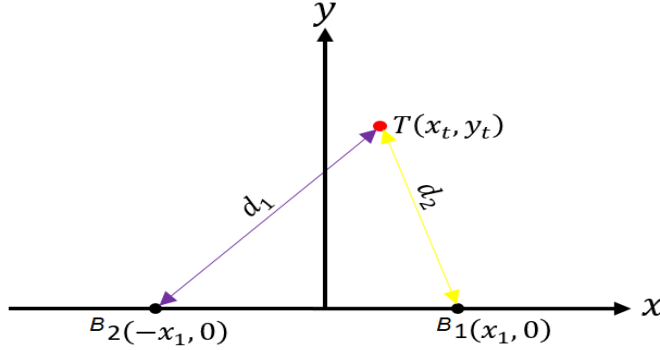


Figure 2.12. 2-Beacons case study: specific case of symmetric positions with respect to the axis  $y$ .

the target node and the beacon node can be written as:

$$\begin{cases} \sqrt{(x_t - x_b)^2 + y_t^2} - \sqrt{x_t^2 + (y_t - y_c)^2} = v \delta t_{bc} \\ \sqrt{(x_t - x_b)^2 + y_t^2} - \sqrt{x_t^2 + y_t^2} = v \delta t_{ba} \end{cases} \quad (2.21)$$

where  $v$  indicates the sound speed and  $\delta t_{bc}$ ,  $\delta t_{ba}$  the time differential of the signal arrival from the beacons B, C and B, A, respectively. As the beacon position is known and the TDoA can be measured, the position target coordinate can be computed by the equations system in (2.21).

In this prototype, only two beacons were available; if the beacon positions are those indicated in Fig 2.12, the following equations can be stated:

$$\sqrt{(x_t + x_1)^2 + y_t^2} = d_1 \quad (2.22)$$

$$\sqrt{(x_t - x_1)^2 + y_t^2} = d_2 \quad (2.23)$$

$$\delta t_{12} = \frac{d_1 - d_2}{v} \quad (2.24)$$

where  $\delta t_{12}$  indicates the TDoA by beacon1-2.

Subtracting the squares of equations (2.22), (2.23), the target position  $x_t$  can be computed from the distances  $d_1$  and  $d_2$ , as well as the beacon

position  $x_1$ :

$$x_t = \frac{d_1^2 - d_2^2}{4x_1} \quad (2.25)$$

Supposed that the target can be found only for  $x_t, y_t > 0$  and subtracting the equation (2.22) to the equation (2.23) combined with the equation (2.24), the target position can be expressed in function of TDoA and the position  $x_t$  or  $y_t$ :

$$y_t = \sqrt{\left(\frac{4x_t x_n - ds^2}{2ds}\right)^2 - (x_t - x_n)^2} \quad (2.26)$$

$$x_t = \sqrt{\frac{ds^2(x_n^2 + y_t^2 - 0.25ds^2)}{4x_n^2 - ds^2}} \quad (2.27)$$

where  $ds = v \delta t_{12}$ .

The deviation of the measured position from a given reference was computed by the following algorithm:

1. The distances  $d1$  and  $d2$  were measured and the coordinate  $x_{tref}$  was determined by the equations (2.25). Using the  $d1$  and  $d2$  in the equation (2.24) and multiply by  $v$ , the  $ds_{ref}$  is determined. Using the  $x_{tref}$  and the  $ds_{ref}$  in the equation (2.26), also the coordinate  $y_{tref}$  is determined. The coordinated  $x_{tref}$  and  $y_{tref}$  are computed using the measures  $d1$  and  $d2$  as references for the experiment. Thereby, the references target position can be indicated as  $P_{tref}(x_{tref}; y_{tref})$ .
2. The value of TDoA  $\delta tp_{12}$  returned by the prototype was used to compute the measurements position using the equations (2.26), (2.27), and the reference position computed at the previous step. In particular, the  $x_{tref}$  and the  $\delta tp_{12}$  in the equation (2.26) gave the value of the measured coordinate  $y_{meas}$ ; in a similar way, the  $y_{tref}$  and the  $\delta tp_{12}$  in the equation (2.27) gives the value of the measured coordinate  $x_{meas}$ .

In this way, the position measurements error can be assessed:

$$\begin{aligned} x_{error} &= x_{tref} - x_{meas} \\ y_{error} &= y_{tref} - y_{meas} \end{aligned} \quad (2.28)$$

### 2.3.5 Experimental results

$d_1$ [m]	$d_2$ [m]	$\bar{x}_{error}$ [cm]	$\bar{y}_{error}$ [cm]	$\sigma\bar{x}_{error}$ [cm]	$\sigma\bar{y}_{error}$ [cm]
2.22	1.82	2.80	-6.9	0.05	0.1
2.28	2.00	-2.3	7.9	0.1	0.4
2.00	1.64	-0.78	2.1	0.06	0.2
2.23	2.00	-0.80	3.4	0.09	0.4

Table 2.2. Measurements results.

The performance of the prototype was tested in an area of  $1.8\text{ m} \times 2.0\text{ m}$  for four different target positions. Two synchronized emitting beacon nodes were positioned at the coordinate  $x_1 = 0.5\text{ m}$  for the coordinate reference system of Fig.2.12.

The measurements were divided into three main phases: positioning, TDoA demonstrator measurements, and positioning error computing.

During the positioning phase, the receiver node was positioned at a generic point  $P_{tref}(x_t; y_t)$  and the distance  $d_1$  and  $d_2$  (Fig.2.12) were measured by a stick meter.

During the TDoA measurements phase, the two synchronized beacons emitted a different frequency sine wave. The beacon1 sent four  $f_1 = 25\text{ kHz}$  sine burst and the beacon2 seven sine burst at  $f_2 = 50\text{ kHz}$ .

Beacon1 and beacon2 were synchronized through a common driving trigger signal. The common signal trigger connected to the two beacons was provided by a third function generator, Agilent 33220A. The function generator sent twenty consecutive trigger signals at a rate  $f_r = 1\text{ Hz}$ . Thereby, after the function generator was started, the receiver node measured the TDoA and the sequence of beacon arrival.

After the TDoA measurements, the results were elaborated using a Matlab<sup>®</sup> code in order to compute the mean and the standard deviation of the position error.

The demonstrator was tested for four different points considering twenty consecutive measures; the results are illustrated in Tab.2.2.

The  $x$  RMS error was  $1.90\text{ cm}$ , the  $y$  RMS error was  $5.59\text{ cm}$  and, the maximum of the error standard deviation was  $0.4\text{ cm}$ .

The presented prototype allowed to gain experience on the US technology, but required a lot of time to develop a fully IPS. For this reason, a commercial ranging module based on UWB technology was used for the IPS and then the  $\beta_{bias}$  estimation.



Figure 2.13. The *DecaWaveDW1000* module with custom PCB interface circuits.

## 2.4 UWB based proposal IPS

Several commercial UWB kits are nowadays available for solutions developers and researcher labs. The chosen system is the commercial *DecaWaveDW1000* modules (Fig.2.13) [92]. The *DecaWaveDW1000* is a module configurable as a beacon or a tag. Thanks to the UWB technology and an ASIC circuit, the module can give us a distance measurement between the beacons node and the target node. The two-way ranging configuration, return the distance measured by the ToF technique. The two-way ranging operation mode can be summarized in three steps Fig.2.14:

1. Communication is established by the tag that sends its address, the destination anchor address and the type of frame. The tag saves the current time stamp  $T_{s_0}$  and waiting for a response from the addressed beacon.
2. The addressed beacon saves the current time stamp  $T_{r_0}$  and answer to the tag with the current timestamp  $T_{r_1}$ .
3. When the tag receives the beacon time stamp message, it saves the current time stamp  $T_{s_1}$  and sends it to the beacon for the last time the time stamp  $T_{s_1}$ . The beacon node saves the current time stamp  $T_{r_2}$  when receive the message.

In this way the ToF can be written as follows:

$$ToF = \frac{(T_{s_1} - T_{s_0}) - (T_{r_1} - T_{r_0}) + (T_{r_2} - T_{r_1}) - (T_{s_2} - T_{s_1})}{4} \quad (2.29)$$

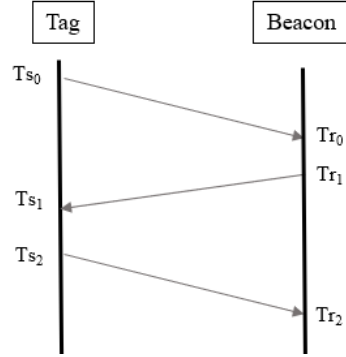


Figure 2.14. The two-way ranging timing and operation schematization.

Considering the 2D study case, the target position was computed by the trilateration algorithm using the Extended Kalman filter (EKF) [93]. Kalman's filter consists of a set of mathematical equations which implement a corrective predictive estimator. The estimate of the state  $X$  of a dynamic system perturbed by noise is carried out starting from a series of measures which are a function of the state itself, but corrupted by additive white noise.

Considering the state equation of a discrete time invariant controlled process:

$$X_k = A \cdot X_{k-1} + B_k \cdot u_k + W_k \quad (2.30)$$

with the measurements equation:

$$D_k = H \cdot X_{k-1} + V_k \quad (2.31)$$

The random variables  $W_k, V_k$  represent the process and measurement noise (respectively). They are assumed independent white and following a normal probability distributions, thereby, the covariance matrix is diagonal.

$$W_k = \begin{bmatrix} \sigma_w^2 & 0 \\ 0 & \sigma_w^2 \end{bmatrix} \quad V_k = \begin{bmatrix} \sigma_v^2 & 0 \\ 0 & \sigma_v^2 \end{bmatrix} \quad (2.32)$$

Where  $\sigma_v$  is the measurements noise and  $\sigma_w$  the model noise. The vector  $u_k$  is the control input, not present in the IPS system description. The estimated state  $X_k = [x_t, y_t]^T$  is the target 2D position at the discrete time  $k$ , while the measured distance between the beacon node and the

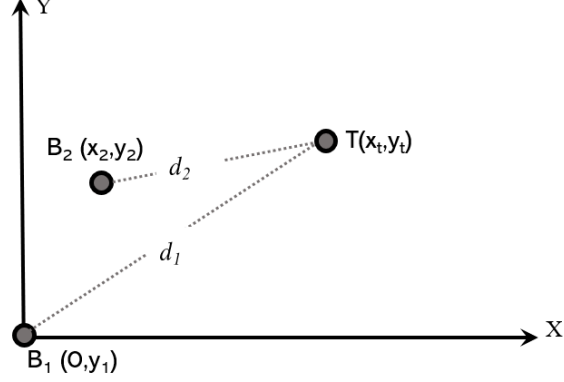


Figure 2.15. Trialteration problem in 2D.

target are the measurements inputs  $D_k = [d_1, d_2]^T$  (Fig.2.15). The matrix  $A$  is the state transition matrix. The matrix  $H$  relates the state to the distance measurement.

The distance between the beacons  $B1$  and  $B2$  and the target node position  $P(x_t, y_t)$ , can be written as follows:

$$\begin{cases} \sqrt{x_t^2 + y_t^2} = d_1 \\ \sqrt{(x_t - x_2)^2 + (y_t - y_2)^2} = d_2 \end{cases} \quad (2.33)$$

The equation (2.33) represents the non-linear measurements equation. According to the EKF theory, the Jacobian matrix  $H$  is considered in the system model [94, 91]. The system model is:

$$\begin{cases} X_k = AX_{k-1} + w_k \\ D_k = HX_k + v_k \end{cases} \quad (2.34)$$

The matrix  $A$  is the state transition identical matrix, and the  $D_k$  vector is the measurements distance at time  $k$  provided by the UWB system.

The Jacobian matrix results from the measurements equation (2.33) linearization:

$$H = \begin{bmatrix} \frac{x_t}{\sqrt{x_t^2 + y_t^2}} & \frac{y_t}{\sqrt{x_t^2 + y_t^2}} \\ \frac{x_t - x_2}{\sqrt{(x_t - x_2)^2 + (y_t - y_2)^2}} & \frac{y_t - y_2}{\sqrt{(x_t - x_2)^2 + (y_t - y_2)^2}} \end{bmatrix}$$

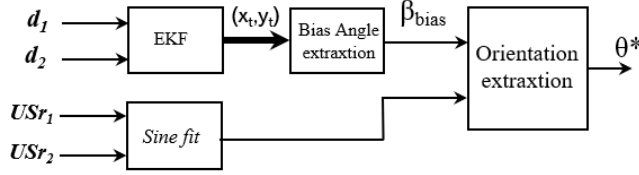


Figure 2.16. The measurements chain. Fusing the UWB position measurements and the US heading information the position and orientation of the LF are known.

Apply the EKF, the filtered target position results from the UWB distance. As previously discussed in section 1.1.1, three beacons are needed in order to track the position. Actually, the EKF returns one of the intersection of the circumference (Fig.2.11), assuming that the target can be only in the positive plane of the FR, the module of the position was considered. The proposed method can track the position and the heading of a target. The 2D case study can be generalized in the 3D space, introducing another more beacon (track to subsection 1.1.1).

## 2.5 Simulation results

The proposed UWB and US fusing method is validated by simulation. The measurements chain can be summarized as in Fig. 2.16. The sine-fit algorithm computes the angle from the US received signal as indicate in the subsection 2.2.2. The EKF estimates the target position and then the  $\beta_{bias}$  correction applies to the eq. (2.10).

The complete fusion algorithm was implemented in Matlab<sup>®</sup> in order to test the tracking performance in presence of Additive White Gaussian Noise (AWGN). Observing the equation (2.9) the heading uncertainly has two contribute, one from the  $\beta_{bias}$  estimation and another from the US heading measurements. The different contribution can be studied separately. The US uncertainly contribute was considered at the first.

For the received US signal, the damped sinusoidal model was assumed eq.(2.20). With  $T = 250 \cdot 10^{-6} s$ ,  $m = 2$ , and  $f_0 = 25 kHz$ . For the simulation phase, a sample frequency of  $f_s = 500 kHz$  and a Signal to Noise Ratio (SNR) of  $SNR = 40 dB$  for the received signal were considered. The USrs receiver distance was assumed  $d_{us} = 5 mm$  according to the condition in the eq.(2.7).

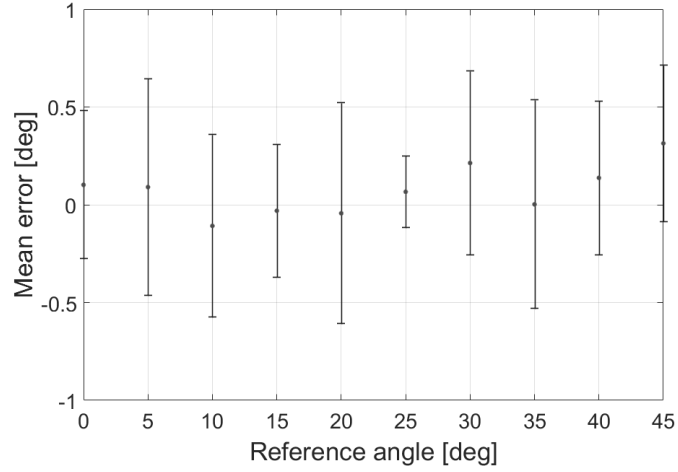


Figure 2.17. Heading estimation mean error and standard deviation bar plot.

Ten consecutive measurements were considered for the same orientation with a fixed  $\beta_{bias} = \frac{\pi}{2}$ . The measurements range was from 0 to 45 [deg] with a 5 [deg] step. In Fig.2.17, the mean error and the standard deviation bar plot are sketched. The error is the difference with respect to the ideal angle and the estimated angle. The maximum mean error is  $\varepsilon_{\theta_{us}} = 0.31 \text{ deg}$  with a  $\sigma_{\theta_{us}} = 0.57 \text{ deg}$  as standard deviation.

The  $\beta_{bias}$  uncertainly contribute was computed considered different target position in the FR. A grid of nine different position were considered. A rectangular shape for the grid was considered Fig. 2.18. Two beacons are in the coordinate  $B1 = (0, 0)$ ,  $B2 = (1.3, 3)$  of the FR. Ten consecutive measurements were considered for each position, the  $\beta_{bias}$  uncertainly contribute and the target position uncertainty are evaluated.

According to the *DecaWaveDW1000* specification, for the measurements noise, a standard deviation of  $\sigma_v = 10 \text{ cm}$  was assumed for the  $v_k$  [95]. For the process noise, the assumed covariance was  $\sigma_w^2 = 0.0004 \text{ m}$ .

In Fig.2.18, the reference grid positions and the EKF estimations are sketched. The mean position difference between the reference position and the EKF output is  $\varepsilon_{EKF} = 11.5 \text{ cm}$  with a  $\sigma_{EKF} = 5.0 \text{ cm}$  standard deviation.

In Fig.2.19, the mean error beta bias error for any grid position of

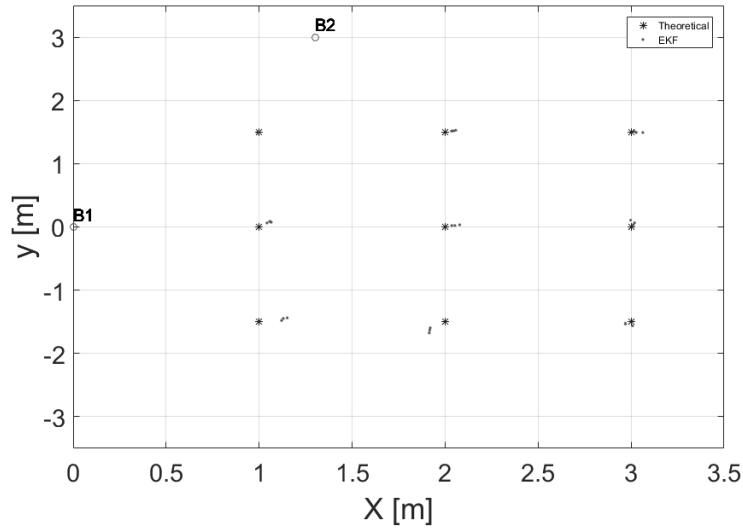


Figure 2.18. Matlab<sup>®</sup> EKF simulation result for  $\beta_{bias}$  and positioning estimation. The reference position in (\*) and the EKF position estimation (·) points.

the Fig.2.18 is sketched. The maximum mean error is  $\varepsilon_{\beta_{bias}} = -1.1 \text{ deg}$ , with a  $\sigma_{\beta_{bias}} = 1.2 \text{ deg}$  standard deviation. The error is defined as the difference with respect to the ideal angle computed using the reference position coordinate and the estimated angle using the EKF position output.

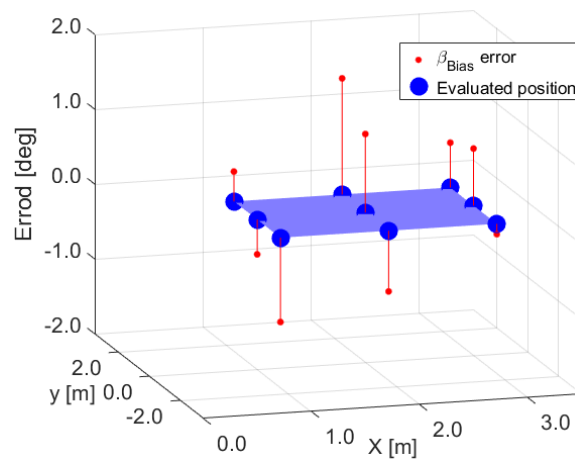


Figure 2.19. Plot of the beta bias error considering the same position data computed in the 2.18.

## Chapter 3

# Results

The US heading measurements system discussed in section 2.2.1 has been designed and prototype in order to validate the theoretical aspect and the metrological performance. Different sensors are present in the market with several characteristics, the eq. (2.7) fixes the dimension boundary for the required USrs [82]. The minimum order USrs is two. As discuss in subsection 2.2.2 the simple 3pSF can be applied for the  $\delta_t$  estimation, but, the frequency must be known with high accuracy and precision. Even low harmonic distortion is required for the acquired signals [96]. Resonant transducers were chosen in order to reduce the harmonic distortion. The resonance frequency  $f_r$  is related to the eq. (2.7) combined with the commercial USrs dimension available. The MEMS technology process offers small microphone in the range of 2 – 3 mm dimension. For a resonance frequency of  $f_r = 25 kHz$ , corresponds a wavelength  $\lambda = 14 mm$  at room temperature, the maximum distance is 7 mm.

### 3.1 Ultrasonic Heading prototype

The principal components of the US heading system are the US transmitter node and the receiver board. The transmitter node generates an US wave at the resonance frequency, the receiver board transduces the US wave in an electrical signal.

The critical component is the receiver node, because of its mechanical and electrical constraint. Low power and low noise circuits are required. In this way, the integration with the common low-power electronics in-

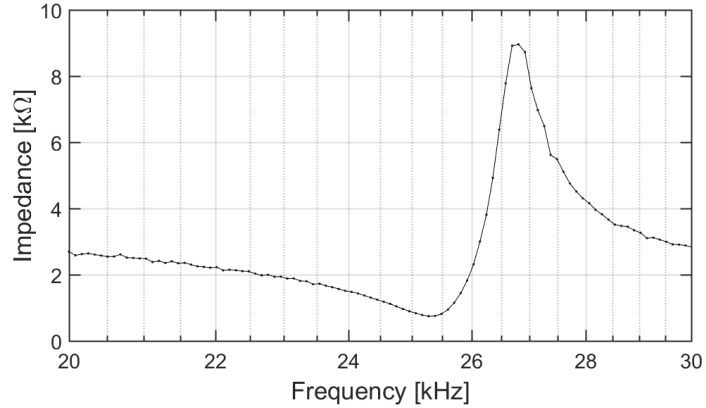


Figure 3.1. The Prowave 250ST160 module of the measured impedance. The minimum module of the impedance is  $|Z| = 0.75 \text{ k}\Omega$  at  $f_r = 25.4 \text{ kHz}$ .

tegrated circuit (i.e., microcontroller) is easy and a portable device can be easily performed [97, 98].

### 3.1.1 Ultrasonic transmitter

The US transmitter Prowave 250ST160, was selected as its center frequency of  $25 \text{ kHz}$  according to the chosen resonance frequency [10]. The 250ST160 is a low-cost piezoelectric transducer.

Piezoelectric transducer uses a mechanical phenomenon called piezoelectricity that converts the mechanical tension in the material in to an induced voltage and vice versa. These transducers are designed to vibrate more efficiently at a specific frequency (resonant frequency). To achieve the maximum efficiency, the transmitter should be driven at their resonance frequency. Usually, this family of sensor requires a medium or high-voltage driving [91]. The small bandwidth of the emitters guarantee a good performance in terms of harmonic distortion.

In Fig.3.1, the transmitter sensor module of impedance frequency response is sketched. The resonance frequency corresponds to the minimum of the impedance module [99]. The experimental resonance frequency is  $f_r = 25.4 \text{ kHz}$ . The bandwidth is about of  $1.5 \text{ kHz}$ , and  $85 \text{ deg}$  total beam angle ( $-6 \text{ dB}$ ).

The maximum sensor driving applicable voltage is  $V_{max} = 20 \text{ V}_{rms}$ .

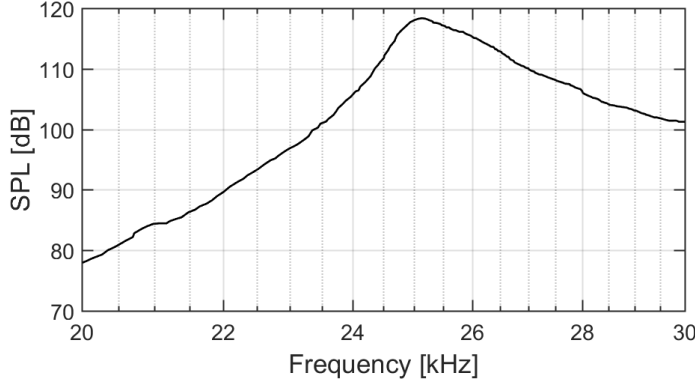


Figure 3.2. The Prowave 250ST160 SPL referred to  $0.0002 \mu\text{bar}$  for  $10 V_{rms}$  at  $30 \text{ cm}$  considering different driving frequency. The maximum of the SPL is at the resonance frequency ( $25 \text{ kHz}$ ) [10].

The emitter aperture is of  $D = 13.5 \text{ mm}$ , applying the condition (2.4), the minimum far-field distance is equal to  $12 \text{ cm}$ .

An important emitters characteristics is the Sound Pressure Level (SPL) measurements [39]. The SPL is the pressure measured within the wave relative to the surrounding air pressure (reference sound pressure) and commonly measured in units of  $\text{Pa}$ . The SPL is given by:

$$SPL = 20 \log \left( \frac{P}{P_0} \right) \quad (3.1)$$

where  $P$  is the sound pressure and  $P_0$  the reference sound pressure. The commonly used reference sound pressure is  $20 \mu\text{Pa}$  or the equivalent in bar,  $0.0002 \mu\text{bar}$  [100].

Usually, the supplier provides the sound pressure SPL in  $\text{dB}$  considering a reference sound pressure, a reference sensor driving voltage magnitude and a fixed distance where the pressure  $P$  is also measured. Then it is possible to compute the SPL at any distance from the sensor and for any driving voltage Fig. 3.2.

Similarly to the eq.(3.2), the driving voltage SPL gain effect is equal to:

$$SPL_{dGain} = 20 \log \left( \frac{V_{dr}}{V_{ref}} \right) \quad (3.2)$$

Where  $V_{dr}$  is the rms sensor driving voltage, and  $V_{ref}$  the rms driving

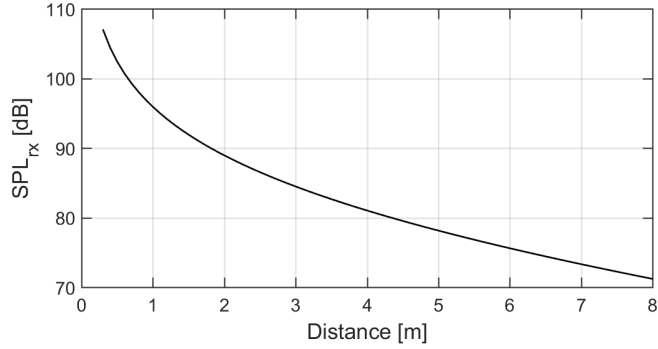


Figure 3.3. The estimated SPL Prowave 250ST160 emitter, varying the sensor distance considering  $V_{dr} = 2.83 V_{rms}$  driving voltage. The SPL was estimated thanks to the transducer supplier information.

reference voltage applied when the SPL was measured.

The SPL of ultrasonic waves created by the transducer is inversely proportional to the distance. In the simplest case of a sound source radiating equally in all directions, the intensity decreases according to the square of the distance [39]. As mentioned before, US transducer specifications provides the SPL at a reference distance from the transducer.

The generic expression of the SPL emitted from the transducer, at the distance  $d$  from the emitter, and for a generic driver voltage  $V_{dr}$ , supposing the measurements point faced to the sensor, is equal to:

$$SPL_{rx}(d, V_{dr}) = SPL(d_0, V_{ref}) - 20 \log\left(\frac{d}{d_0}\right) + 20 \log\left(\frac{V_{dr}}{V_{ref}}\right) - \alpha(d - d_0) \quad (3.3)$$

The first terms  $SPL(d_0, V_{ref})$  is the SPL provided from the supplier at reference distance and driving voltage. The second term represents the power loss because of the spherical divergence. The third term is the driving voltage SPL gain (eq.(3.2)). Finally, the fourth term is the power loss because of the air absorption. A proportion of the wave energy is converted to heat when travels through the air. The term  $\alpha$  is the absorption coefficient (expressed in dB/m), function of the sound wave frequency and air temperature.

The 250ST160 transducer offers a SPL of  $SPL(d_0 = 0.3 \text{ m}, V_{ref} =$

10  $V_{rms}$ ) = 118 dB (Fig.3.2). Assuming the air temperature of  $T_{air} = 25 C^\circ$  and the frequency work of  $f_{res} = 25 kHz$ , the air absorption is equal to  $\alpha = 0.95 dB/m$ . In Fig.3.3, the SPL value at varying distance is sketched, considering the Prowave 250ST160 emitter characteristics, and the previously reported air absorption value [10].

For the preliminary test, the driving circuit was supplied by the Arbitrary Waveform Generator Agilent 33220A and it can be easily replaced with a low power portable oscillator. The required power can be easily computed as:

$$P_{Diss} = \frac{V_p^2 \cos(\varphi)}{2 |Z|} \quad (3.4)$$

where  $V_p$  is the voltage driver peak value,  $\varphi$  and  $|Z|$  are respectively the phase and the module of the impedance, evaluated at the driving frequency. For the Prowave 250ST160 emitter, the measured phase is equal to  $\varphi = -65 deg$  and  $|Z| = 867 \Omega$  at the frequency of  $f_{res} = 25 kHz$ . The required power is equal to  $P_{Gen} = 3.9 mW$ .

### 3.1.2 Receiver node

The receiver node has two boards, the *transducer board* and the *filter board*.

The *transducer board* holds two MEMS ultrasonic transducers. The minimum distance between the USrs transducer must be less than (eq.(2.7)):

$$d_{min} = \frac{\lambda}{2} \simeq 7 mm \quad (3.5)$$

The chosen MEMS USrs transducer are the SPU0410LR5H [11]. Thanks to the small dimension (L=3.76 mm, W=3.00 mm, H=1.10 mm), the SPU0410LR5H was used as USr. The microphone input apertures was placed at the distance of  $d_{US} = (4.9 \pm 0.2)$  mm following the process tolerance, in order to guarantee the phase ambiguity condition in eq. (2.7).

The SPU0410LR5H is low power general purpose capacitive microphone used in cellphones, smart phones, laptop computers etc. This sensor can be used in the audible bandwidth and in the US domain. One of its main feature is the sensitivity. The sensitivity is the electrical response at the sensor output to a given standard acoustic input. This is expressed by the ratio of the input pressure with respect to the elec-

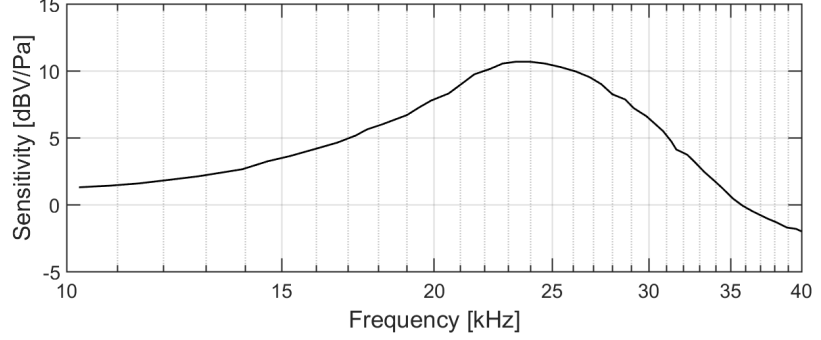


Figure 3.4. The SPU0410LR5H sensitivity response normalized to 1 kHz [11]. The increase in sensitivity at  $f_r = 25 \text{ kHz}$  with respect to the normalized frequency is equal to 10.4 dBV/Pa.

trical output, considering a reference input SPL. The suppliers usually consider the standard reference input of 1 kHz sine wave at 1 Pa SPL, providing the value expressed in dBV/Pa:

$$S_{rx} = 20 \log \left( \frac{V_{OUT}}{P_{ref}} \right) \quad (3.6)$$

where  $S_{rx}$  is the sensitivity value,  $V_{OUT}$  the sensor output voltage and,  $P_{ref}$  the reference SPL. Since the manufacturer provides the measured  $S_{rx}$  value at the  $P_{ref}$  (usually equal to 1 Pa), the sensors voltage output can be easily computed if the SPL at the microphone input is known, inverting the equation Equation 3.6 multiply by the received SPL:

$$V_{rx} = P_{rx} P_{ref} 10^{\left(\frac{S_{rx}}{20}\right)} \quad (3.7)$$

where  $V_{rx}$  is the sensor output voltage and,  $P_{rx}$  is the received SPL at the input of the microphone.

The term  $P_{rx}$  can be computed by combining the eq.(3.1) and eq.(3.3) in particular, is equal to:

$$P_{rx} = P_0 10^{\left(\frac{SPL_{rx}(d, V_{dr})}{20}\right)} \quad (3.8)$$

According to the Prowave 250ST160 specification, the  $P_{rx}$  can be calculated considering the reference pressure value of  $P_0 = 20 \mu\text{Pa}$ , in this

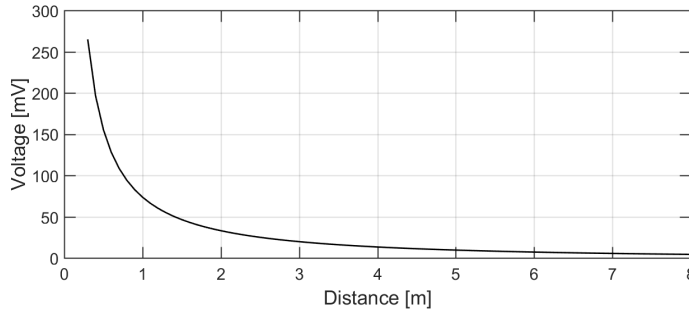


Figure 3.5. The SPU0410LR5H estimated receiving rms output voltage considering the Prowave 250ST160 emitter driven by a  $V_{dr} = 2.83 V_{rms}$ .

way, the  $P_{rx}$  is expressed in pascal and it can be used in the eq. (3.7). The SPU0410LR5H sensitivity frequency response presents a resonance peak at frequency  $f_{SP} = 25 kHz$  matching with the transmitter resonance peak Fig.3.4.

The SPU0410LR5H  $S_{rx}$  is equal to  $-38 dB/Pa$  (the typical value) considering  $1 kHz$  and  $1 Pa$  SPL as input ultrasonic wave [11]. Stated the SPU0410LR5H sensitivity response in the Fig.3.4, the equivalent sensitivity value at the working frequency of  $f_r = 25 kHz$  is equal to  $S_{rx}(25 kHz) = -27 dB/Pa$ .

In the Fig.3.5, the MEMS output voltage at varying distance considering the MEMS and the US emitter specification is sketched. The SPU0410LR5H acoustic overload point is equal to  $118 dB$  SPL. The overload point defines the maximum input SPL that guarantees less than 10% of Total Harmonic Distortion (THD). According to the Fig.3.3, the driver voltage of  $V_{dr} = 2.83 V_{rms}$  guarantee the acoustic overload point condition and then the low harmonic distortion required to the 3pSF algorithm. The *filtering board* implements two identical filters for each microphone. A single voltage power supply filter was designed. In Fig.3.6, the filter schematics of one channel is sketched. The filter was a dual-stage 4<sup>th</sup> order Chebyshev pass-band filter, with a central band gain of 14 dB at 25 kHz and a pass band  $f_B$  of 3 kHz. The voltage power supply was  $V_{CC} = 3.3 V$  according to the low power requirements and the USr required supply voltage. The OP AD8031 [101] mounted in buffer configuration, provides the mid-supply reference voltage  $V_{ref} = \frac{V_{CC}}{2}$  for the filter section. The circuit provided a low-impedance reference voltage, in order to attenuate the interference with the filter frequency

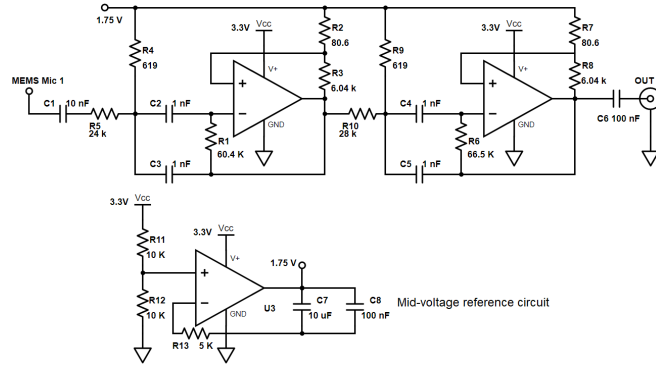


Figure 3.6. The single channel analog filter and voltage reference circuits schematics. The same circuit was duplicate for the second sensor.

response. The AD8031 [102] is a single chip for channel OP used for the Chebyshev pass-band filter implementation. During the production, particular attention was paid to the layout symmetry in order to balance the delay in the two channels.

### 3.1.3 Realization

The printed circuit was designed and assembled using surface mounted package in order to reduce the parasitic components and the total size. The two boards (filtering and transducer board) were a double face 3.5 mm FR4 Printed Circuit Board (PCB). The transducer board dimension was  $L_t = 20$  mm,  $W_t = 15$  mm,  $H_t = 2$  mm; the filtering board dimension was  $L_f = 80$  mm,  $W_f = 40$  mm,  $H_f = 5$  mm. The filter boards were provided with two female BNC connectors in order to allow a shielded connection with the measurements station.

## 3.2 Low cost electronic goniometer

The heading accuracy of the proposed system needs to be experimentally evaluated. For the metrological performance evaluation, a reference heading measurements systems is necessary. For this reason, an Accurate low-cost Electronic Goniometer was prototyped. After the metrological characterization, the goniometer was used for the metrological characterization of the US proposed heading system, thanks to an isolated rotating

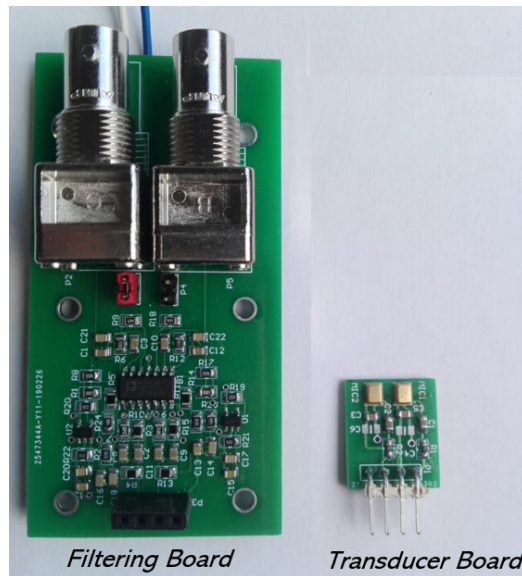


Figure 3.7. The filtering and transducer complete board. The total size of the filtering board can be halved if BNC connectors are removed

plate on which the receivers can be placed.

The general idea of the Electronic goniometer (EG) is to transduce the mechanical rotation in an electrical parameter variation, like the resistance variation.

### 3.2.1 Realization

The principal components of the EG are the rotating plate and the precision potentiometer. The center of the plate was in turn keyed to the shaft of the precision potentiometer. The plate was made of Teflon to be light thanks to a lathe process. During the assembly, particular attention was paid to verify that the shaft center coincided with the center of the sensor board. The plate joint with the boards and the potentiometer shaft, could rotate by an angle at user's will. A plate rotation of  $\theta$  angle corresponds exactly of a potentiometer  $\theta$  rotation (1:1 coupling ratio). Apply the calibration method, the measured resistance linearly depends on rotation. The potentiometer is a ten turn linear precision potentiometer of  $2\text{ k}\Omega \pm 3\%$  resistance, with a 0.25% linearity. The potentiometer was housed in a teflon cylinder and was free to slide along

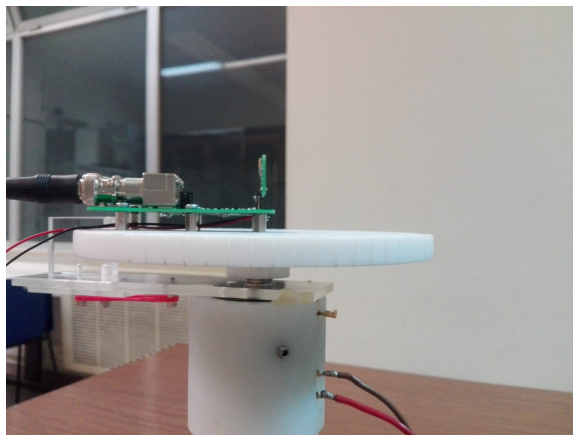


Figure 3.8. The plate and the potentiometer goniometer prototype. The plate can rotate in clockwise and anticlockwise, in this way an arbitrary heading angle can be chosen for the measurements.

a grooved bar to change the position. In particular, the EG can shifting in one direction (e.g x axis).

A slider positioned below the teflon cylinder base was helpful to prevent lateral movements during the positioning; therefore, the system was stabilized and does not suffer from significant angular torsions. In this way, only the plate could rotate by an estimated angle during the measurements. In Fig.3.8, there is the prototype with the mounted filter board.

### 3.2.2 Metrological characterization

The inverse calibration model is used to get the reference angle. The mechanical angle measurements system was characterized using an automatic test equipment based on the multimeter Keythley 2000 used as ohmmeter in order to measure the potentiometer resistance. A LabView<sup>®</sup> software was developed in order to control the multimeter via the IEEE 488 interface.

A mechanical reference system was used in order to place the plate at the reference angle. During the plate manufacturing, a 5 degrees steps cuts was made. The aim of the cuts is to block the plate in a fixed known position.

The positioning error on the plate circumference is  $\delta_p = (1.0 \pm$

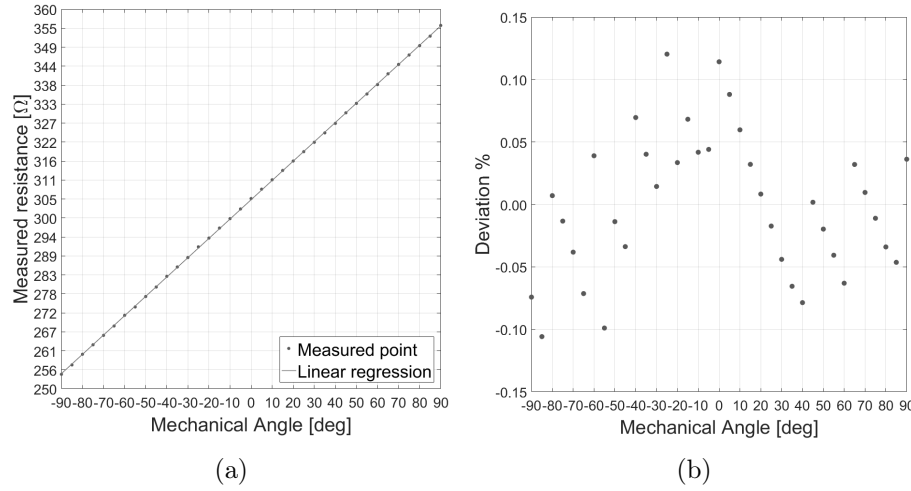


Figure 3.9. (a) Measured resistance point and the linear regression. (b) Percentage deviation.

0.1) *mm*. The positioning error and its uncertainty have effects on the plate angle error and uncertainty. The angle error depends on the plate's diameter and positioning uncertainty. The plate's diameter was measured by a caliper  $d = (162.5 \pm 0.1)$  *mm*. The angular error can be easily evaluated, namely:

$$\epsilon_{angle} = 2 \arcsin \left( \frac{\delta_p}{d} \right) \quad (3.9)$$

Applying the uncertainties propagation law in indirect measurements (uniform pdf) the angle error is:  $\epsilon_{angle} = (0.70 \pm 0.06)$  *deg* with a 5 degrees resolution.

The mechanical plate rotation system was used for the reference angle positioning during the measurements. For each plate step rotation, 32 resistance measures were carried out. Starting from these measurements, a type A evaluation of uncertainty was assessed; moreover, using the accuracy specifications provided by the manufacturer, a type B evaluation was done.

Expanded combined uncertainty and a coverage factor  $k=2$  [103] was chosen, and the procedure was repeated 36 times to resolve half circumference.

The  $\chi^2$  test for gaussianity verification was applied. The gaussian-

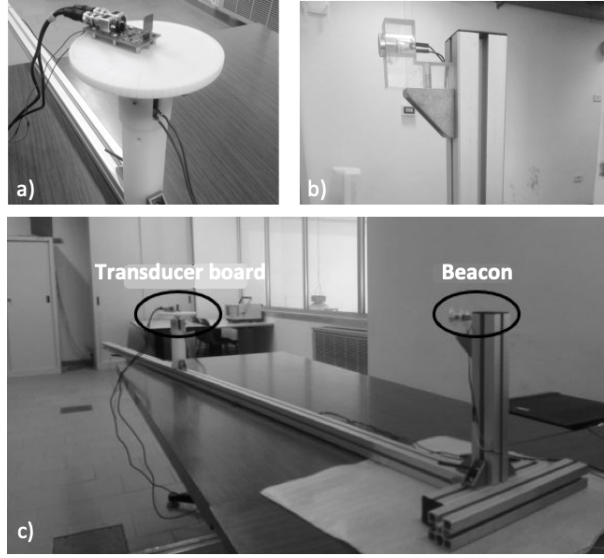


Figure 3.10. Mechanical setup: a) the transducer board on the rotating plate of the reference goniometer, b) the US beacon on the Plexiglas support, and c) the transducer board sliding along a grooved bar at different distances from the beacon.

ity test resulted positive for all measured points. Then the mean, the standard deviation and variance were used to check the linearity of the estimated model thanks to the Fisher-Snedecor test. The results for the prototype developed are shown in Fig.3.9a.

The evaluated  $1\sigma$ -repeatability is less than 0,03%. The evaluated gain and offset coefficients were used to get the measurement of any rotation angle from a single resistance measurement. Using the linear regression model, the measured angle can be obtained from the resistance measurements by the following equation:

$$\phi = \frac{R - \alpha}{\beta} \quad (3.10)$$

Where  $\phi$  is the EG angle estimation,  $\alpha$  is the offset,  $\beta$  the gain, and  $R$  the measured resistance. The following values were assessed for the offset and gain:  $\alpha = 304.57 \Omega$ ,  $\beta = 0.56 \Omega/deg$ . With a maximum percentage deviation of 0.12 %.



Figure 3.11. The measurements station in details: the receivers board mounted on the rotating plate (1), the US transmitter (2), the DSO (3), the waveform generator (4), the ohmmeter (5). The instruments were controlled by a custom Matlab<sup>®</sup> application.

### 3.3 Metrological characterization

For the static test, the transducer and the filtering boards of the US heading system prototype were mounted on the same side of the Teflon plate (Fig.3.10a) of the EG. The ultrasonic wave was generated by the US 250ST160 beacon (Fig.3.10b), supplied by the Arbitrary Waveform Generator Agilent 33220A.

A battery pack was used in order to supply the filter and sensor board. Using two BNC cable, the two signals filter board output, were digitized using the TDS1002 Tektronix DSO at a sampling rate of 10 MSa/s. The waveform generator and the oscilloscope were controlled remotely by a notebook (Intel Core i5 2.70 GHz). In the same notebook, the measurement algorithms ran coded in a Matlab<sup>®</sup> application. The data acquisition from the oscilloscope, the 3pSF and the heading angle extraction algorithm (Table 2.1) were implemented in the Matlab<sup>®</sup> application Fig. 3.11.

The mechanical angles were measured by the EG reference goniometer using the resistance measurements combined with the linear model (eq. (3.2.2)). Finally, the two measurements (the EG and the UHS) were compared to determine measurement heading uncertainty.

The metrological characterization problem can be faced in two different steps: the *geometrical configuration* heading problem definition, and the *mechanical stabilization* of the EG reference.

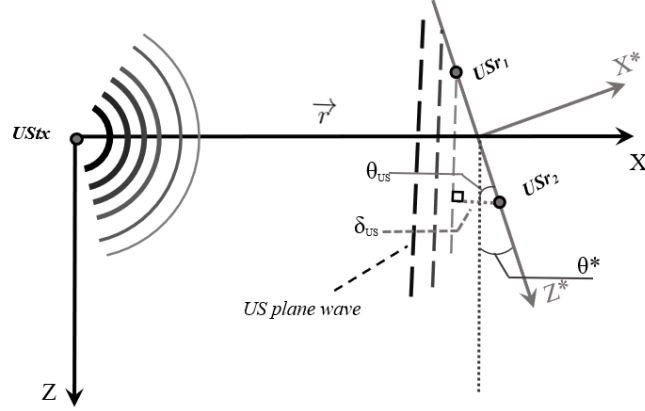


Figure 3.12. Assumptions for US transmitter and receiver: alignment of the origins of the reference frame  $(X, Z)$  and localized frame  $(X^*, Z^*)$ . A positive heading  $\theta^*$  of the localized frame is sketched.

- **Geometrical configuration:** The bias term  $\beta_{bias}$  (2.9) dependency, has been removed in order to measure only the US heading system error of the localized frame. In Fig.3.12, the aligned configuration of the origins for the reference and localized frames is illustrated assuming a positive  $\theta^*$  heading angle. In this case, the biasing  $\beta_{bias}$  is known and equal to  $\frac{\pi}{2}$  rad. The localized frame heading angle  $\theta^*$  is a function of the two distances  $\delta_{US}$  and  $d_{US}$ :

$$\theta^* = \frac{\pi}{2} - \arccos\left(c \frac{\delta t}{d_{US}}\right) \quad (3.11)$$

During the measurement temperature  $(25 \pm 1)$  °C and humidity  $(52 \pm 1)$  RH % were monitored both to comply with the instrumentation operating conditions, and to take into account their influence on the ultrasounds [104, 105].

Only the room temperature was taken into account using the equation for the speed of sound in dry air:

$$c = 20.05 \sqrt{T} \quad (3.12)$$

where  $T$  is the temperature in Kelvin [106].

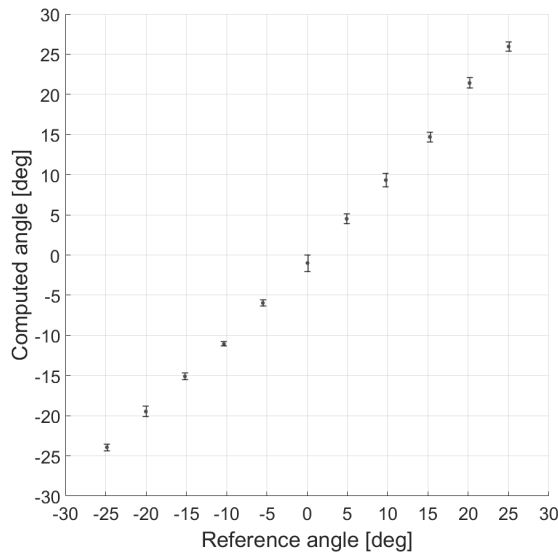


Figure 3.13. Calibration of the US heading system (mean and  $1\text{-}\sigma$  repeatability bar plot) for a beacon-receiver distance of 1.0 m.

- Mechanical stabilization.** The mechanical setup as a whole is illustrated in Fig.3.10c here, the possibility for the transducer board of sliding along a grooved bar at different distances from the beacon can be argued. The ultrasonic transmitter was fixed using a Plexiglas support in order to guarantee the proper alignment. The EG was housed in a Teflon cylinder. The slider positioned below the base prevented lateral movements while approaching to the beacon. Thus, the system was stabilized without any significant angular torsion. In this way, only the plate could rotate by an estimated angle during the measurements.

The tightening torque for the used bolts (M8, metric thread, triangular profile, coarse pitch, and friction coefficient of 1.0) as prescribed by the standard DIN 267-27:2004-01, is equal to 23 N/m and guaranteed by a calibrated torque wrench (max error = 2%).

Referring to the Fig.3.14 the measurements procedure can be summarized as follows:

- Imposition a fixed mechanical rotation at fixed transmitter-receivers distance

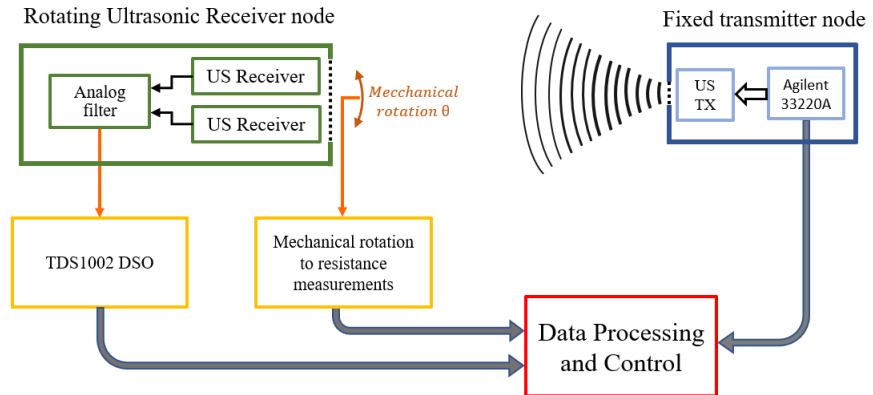


Figure 3.14. The measurements scenario block diagrams.

- Driving the US transmitter with the waveform generator.
- Reading the resistance and convert it in an equivalent angle.
- Acquire the two analog waveform.
- Compute the estimated angle from the UHS.
- Storing the waveform and repeat the measurements procedure.

### 3.3.1 Metrological results

The validation data-set were acquired within the range  $[-25, 25]$  deg by steps of 5 deg. Ten measurements for each step were considered. In Fig.3.13, the reference angle, the average measurements and the standard deviation are sketched for 1 m of beacon-receiver distance.

Because of the tolerance components and the mismatching in the real filters implementation for the two different channel, an offset was present at the output of the filter board.

The offset was measured and compensated. The same sinusoidal signal was considered as input for each filter in order to estimate the output delay offset. The presence of the offset implies a not zero heading measurement also for a null heading angle, because the output signal filter were out of phase even if at the input filters are in phase (offset error).

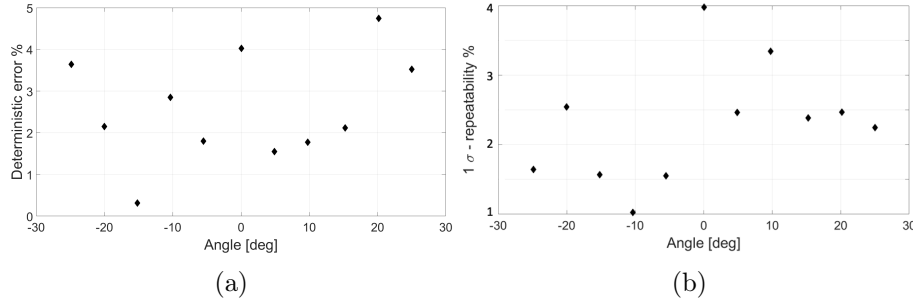


Figure 3.15. (a) The percentage deterministic error versus the measured angle for a beacon-receiver distance of 1.0 m. (b) 1-  $\sigma$  percentage repeatability versus the measured angle for a beacon-receiver distance of 1.0 m.

For this reason, the measured offset was compensated by modeling in eq. (3.13) a time delay  $\delta t_0$  of  $-1.18 \mu\text{s}$ :

$$\theta^* = \frac{\pi}{2} - \arccos\left(c \frac{\delta t + \delta t_0}{d_{US}}\right) \quad (3.13)$$

The deterministic error was computed as the difference between the reference angle measured by the EG and the mean of ten measurements made with the proposed UHS. The percentage deterministic error and the 1- $\sigma$  repeatability were assessed with respect to the maximum measured angle. The percentage error was calculated as:

$$\epsilon\% = 100 \frac{\theta_{ref} - \overline{\theta^*}}{\max(\overline{\theta^*})} \quad (3.14)$$

where  $\theta_{ref}$  is the reference angle,  $\overline{\theta^*}$  the mean of the measured values by the UHS, and  $\max(\overline{\theta^*})$  is equal to  $25.96 \text{ deg}$ .

The maximum deterministic error was  $\bar{\epsilon}_{max} = 1.2 \text{ deg}$  with a  $\sigma = 0.8 \text{ deg}$  standard deviation. The maximum percentage deterministic error was less than 5% ( Fig.3.15a). This error can be compensated by computing its value for a given measurement configuration (calibration). The 1- $\sigma$  repeatability was less than 4% (Fig.3.15b).

Linearity was assessed according to Fisher-Snedecor test with a con-

Nominal bits	Samp.Rate [MSa/s]	THD [%]	SNR [dB]	ENOB
8	5.1	0.3	33.8	5.3
8	10.0	1.4	35.3	5.5
12	1.0	0.3	36.7	5.8
12	5.1	0.2	41.0	6.5

Table 3.1. THD, SNR, ENOB varying the number of bits and sampling rate when the reference angle  $\theta_{ref} = 0$  [deg]

confidence of 95%:

$$\sigma_{NL\%} = \sqrt{\sum_{k=1}^n (\hat{\epsilon}_k - \bar{\epsilon}_k)^2} \cdot \frac{1}{(n-1)} \cdot \frac{100}{(y_{max} - y_{min})} \quad (3.15)$$

where  $n$  is the number of averaged experimental points,  $\hat{\epsilon}_k$  is the  $k$ -th non linearity error,  $\bar{\epsilon}_k$  the average linearity error, and  $y_{min}$  and  $y_{max}$  the lowest and highest level, of the angle. The result  $\sigma_{NL\%}$  below 2%.

### 3.3.2 Noise and distortion analysis

The UHS heading system architecture guaranteed several filtering stages: (i) tuned filtering from ultrasonic beacon and receiver's frequency response (Fig.3.4 and, Fig.3.2), (ii) active fourth-order analog filter on the receiving system, and (iii) the 3pSF algorithm. The THD effect was investigated considering different sampling rate and Analog Digital Converter (ADC) nominal bits. THD analysis results in Table 3.1 highlight a satisfying robustness to distortion.

In the worst experimental conditions of an 8-bit ADC with 1 MSa/s sampling rate, THD resulted less than 5 %. The ADC bit numbers impact on measurement uncertainty in relationship with Signal to Full Scale Ratio (SFSR) and sampling rate. Six different experimental measurement set-ups were tested at varying the sampling rate (1.0 MSa/s, 5.1 MSa/s, 10.0 MSa/s) and the number of bits (8, using TDS1002 Tektronix DSO, and 12 using a microcontroller STM32F303xC). In all the six set-ups, the beacon was powered at 4 Vpp and the receivers were placed at a distance of 1 m. In each condition, the SNR was measured

and then the Effective-Number-Of-Bit (ENOB) was calculated according to IEEE 1057-2007:

$$SNR = 6.02 \cdot ENOB + 1.76 \text{ dB} \quad (3.16)$$

Results are shown in Table 3.1. Even at the condition of minimum ENOB 5.32, namely 8 bits and 5.1 MSa/s, the system keeps uncertainty compatible with experimental set-up of section Sec.3.3.

SNR was analyzed also at varying the distance between beacon and receivers in the range [1 m, 8 m] by steps of 1 m. The experimental signal attenuated progressively according to the signal propagation model, based on the beacon-receiver distance, the ultrasound field divergence [107], and the ultrasonic air absorption at 25 °C (eq.(3.3) and, eq.(3.7)).

The experimental signal was acquired in the following conditions: beacon powered at 4 V<sub>pp</sub>, 1 m of distance beacon-receiver, 3 m of distance from the lateral wall, 8-bit ADC, and 1.0 MSa/s sampling rate. Moreover, a white noise with varying standard deviation [0.05 V, 0.10 V, 0.15 V] was added as further input of the receivers.

In the worst case, 8 m distance and 0.15 V 1- $\sigma$  white-noise, the SNR decayed to 9.1 dB from the initial value of 36.6 dB, and the maximum deterministic error of the heading goniometer in the range [-25, 25] deg increased less than 15% (from 1.2 deg to 1.4 deg in absolute value).

### 3.3.3 Interference Analysis

The analog and digital filters guaranteed an effective rejection to undesired contributions out of the narrow band centered at 25 kHz. However, the reflected waves at 25 kHz affect the heading measurement because of their phase shift. If a reflective surface was present near the USr, the received signal would be composed by two contributes: the direct path and the reflected path (similarly in Fig.1.8). The two paths corresponding to a two different phase and amplitude received signals. The received signal was at the same frequency, resulting in a phase shift and amplitude modulation received signals.

The received signal was the sum of the two signals: direct and reflected, namely:

$$v_{RX}(t) = A_d \cos(2\pi f_s t + \varphi_d) + A_r \cos(2\pi f_s t + \varphi_r) \quad (3.17)$$

where,  $A_d$  and  $A_r$  are the direct and reflected wave amplitude respec-

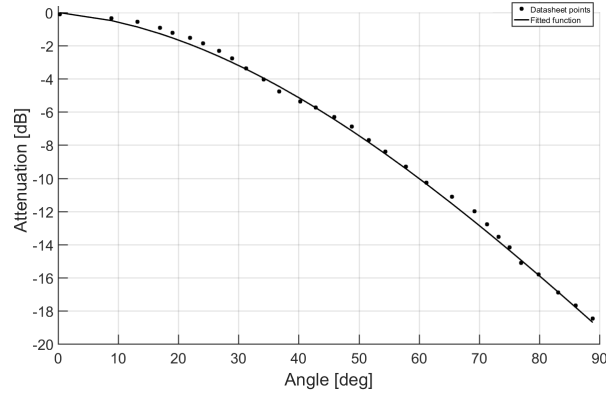


Figure 3.16. The Prowave 250ST160 attenuation functions provided by the supplier ( $\cdot$ ) [10] and, the fitted function ( $-$ ). The attenuation was measured considering the reference distance and driving emitter voltage and rotating the emitter by an angle ( $\phi$ ).

tively and,  $\varphi_d$  and  $\varphi_r$  the direct and reflected wave phase respectively measured at the USr and,  $f_s$  the carrier frequency (25 kHz). The eq.(3.17) represents the generic received signal expression due to the reflection. The eq.(3.17) can be applied for each US receiver, considering the proper phase shift and amplitude modulation.

The phase shift which is the expression of a longer path, depends on (i) the distance between the beacons, the receivers, and the reflective surfaces in the environment, and (ii) the reflection angle determined by the relative inclination of the reflecting surface with respect to the beacon-receiver axis.

The interference also depends on the amplitude of the received reflected wave. The directivity of beacon and receivers, the heading angle  $\theta^*$ , and the reflection angle  $\theta^\#$  modulate the amplitude of the interference.

A custom algorithm implemented in Matlab<sup>®</sup> simulated the UHS output in case of interference due to reflected waves. In particular, the inputs of the algorithm were: (i) the relative distance between beacon receivers and one lateral wall, (ii) the amplitude of wave emitted from the beacon, and (iii) the heading angle  $\theta^*$ . The beacons and the USr where assumed at the same height and then, the geometrical problem can be reduced in a two-dimensional problem (Fig.3.12).

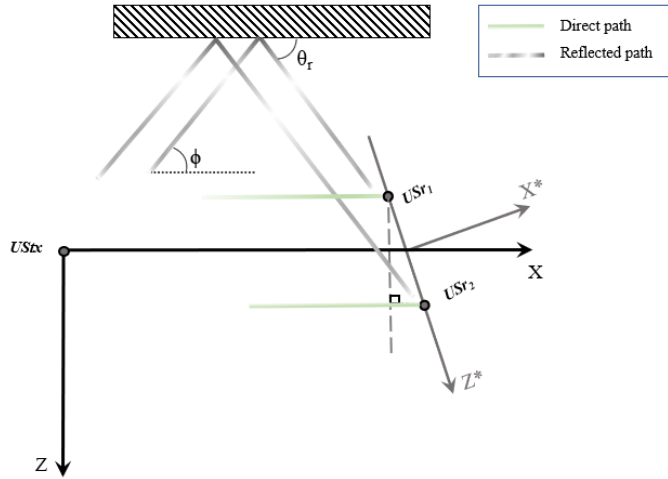


Figure 3.17. The direct and the reflected path and the reflected angle ( $\theta_r$ ). The reflected angle was computed apply the Snell's law. The emitter attenuation related to the ( $\phi$ ) angle and the attenuation function (Fig.3.16).

Because the relative distance between the beacon, receivers and one lateral wall were known, the direct and reflected wave covered distance are know. The Snell's law imposing the equality between the incident angle and the reflected angle. The difference of the two paths ( $\Delta_{Path}$ ), determines the terms  $\varphi_d$  and  $\varphi_r$  in the eq. (3.17). The amplitude terms were related to the covered distance, as seen in eq.(3.3). In the power calculation the absorption of the wall was not considered, assuming the lateral wall an ideal reflector:

$$Z_{wall} \gg Z_{air} \quad (3.18)$$

where,  $Z_{wall}$  and  $Z_{air}$  represent the wall and air acoustics impedance respectively [39].

In the eq.(3.3) the  $SPL(d_0, Vref)$  term is valid, supposing the measurements point faced to the sensor. Because the lateral wall forms an angle with the transmitter and the receiver, the transmitter and received power change in particular, depends on the angle, namely:

p1	p2	p3	p4
8.6 10 <sup>-6</sup>	-0.0028	-0.0307	0.166

Table 3.2. The polynomials fitted coefficients for the Prowave 250ST160 points of the attenuation function in Fig.3.16. Half of the total attenuation angle was considered ( $\phi$  [0:90] deg).

$$SPL_{rx}(d, V_{dr}, \phi) = SPL(d_0, V_{ref}, \phi) - 20\log\left(\frac{d}{d_0}\right) + 20\log\left(\frac{V_{dr}}{V_{ref}}\right) - \alpha(d - d_0) \quad (3.19)$$

where  $\phi$  is the angle formed by the wall and transmitter Fig.3.17,  $SPL(d_0, V_{ref}, \phi)$  is equal to:

$$SPL_{rx}(d_0, V_{ref}, \phi) = SPL(d_0, V_{ref}) + A(\phi) \quad (3.20)$$

where the term  $A(\phi)$  is the attenuation factor in order to taking into account the angle acoustic power dependency in particular, the acoustic power decreasing. In Fig.3.16, the transmitter attenuation points related to the angle dependency was sketched [10]. The effect of the directivity was modeled by introducing the attenuation factor, depending on the angle formed between the direction of maximum directivity (assuming the measurements point faced to the sensor) and the actual angle. The attenuation function was symmetrical, for this reason the modulus of the  $\phi$  was considered. The attenuation function was obtained by fitting the measured points provided in the datasheet by the supplier, assuming a 3rd order polynomial model:

$$A(\phi) = p1|\phi|^3 + p2|\phi|^2 + p2|\phi| + p4 \quad (3.21)$$

the computed coefficient  $p_n$  minimize the least-squares error between the experimental points and the polynomial model in the eq. 3.21. The best-fit considered coefficient value were reported in Tab.3.2 and, in Fig. 3.16 the polynomial fitting function was compared with respect to the experimental points.

Apply the same transmitter consideration for the receivers, in the

	[107]	[108]	[109]	[110]	Proposal
<b>Range [deg]</b>	[-40, 40]	[-5, 5]	[-30, 30]	[-20, 20]	[-25, 25]
<b>Max Error [deg]</b>	<18	<1.5	2	3.6	1.2
<b>Operation Distance [m]</b>	<4	<1	1.5	<4	>7

Table 3.3. Comparison among the proposed system and recent state-of-the-art solutions considering the angular range, the maximum operating distance, and the maximum error.

eq.(3.8) the angle received power dependency was added for the USr outputs voltage calculation. Thanks to the Snell's law, the angle  $\phi$  was computed and the attenuation effect was taking into account. Finally, the SPL considered was a function of the transmitter and receiver directivity, distance and, the attenuation of ultrasound in the air (assumed at 25 °C).

The 8-bit ADC quantization error was taking into account in the implemented custom algorithm in order to model the ADC conversion effect related to the amplitude variation of the received signal (the gain and offset error where not considered for the ADC).

The algorithm outputs were: (i) the incident angle  $\theta^\#$  of the reflected wave on the receivers, (ii) the difference of the paths between the two reflected waves from beacon to receivers ( $\Delta_{Path}$ ), and (iii) the amplitude and phase of the resultant interference. Apply the eq.(3.17) the received signal was calculated, afterwards, the signal was amplified and filtering according to the analog filter response. Finally, the signal was quantized and the 3pSF was applied in order to computed the heading angle.

In Fig. 3.18, black dots indicate the simulated deterministic error at varying the heading angle for  $\theta^*$  within the range [-35, 25] deg. The deterministic error remains below the level of 1.2 deg, when receiver and beacon are at a mutual distance of 1 m and both are 3 m far from a lateral wall. Simulation outcomes are compatible with experimental results. Therefore, the experimental deterministic error below 1.2 deg within the range [-25, 25] deg is well explained by the combined effect of beacon and receiver directivity, as well as the relative position of beacon, receiver, and reflective surfaces. The partial narrowing of the interval in the experimental case is due to the effect of the other walls, much more distant and therefore not modeled by the simulation.

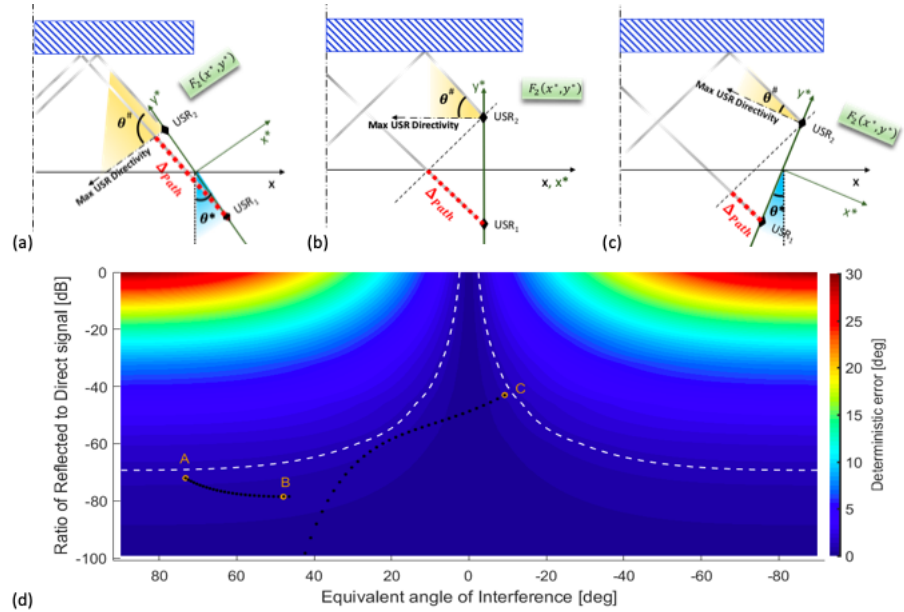


Figure 3.18. Incident angle  $\theta^\#$  of reflected wave at varying heading angle for  $\theta^*$  equal to -35 deg (a), 0 deg (b), 25 deg (c). Deterministic error caused by interference depends on directivity of the receiver and the difference of the paths between the two reflected waves from beacon to receivers ( $\Delta_{Path}$ ). In (d), the Matlab<sup>®</sup> simulation plots of the deterministic error as a function of interference amplitude (y axis) and phase shift (x axis) is reported. The latter is equivalent to  $\Delta_{Path}$ . White line indicates deterministic error of 1.2 deg. Black dots indicate the simulated errors at varying  $\theta^*$  within the range [-35, 25] deg, with a receiver-beacon distance of 1 m, and both of them 3 m far from a lateral wall.

### 3.3.4 Throughput Performance

The computation cost was assessed on a STM32F303xC ArmR<sup>®</sup>CortexR<sup>®</sup>-M4 32-bit microcontroller, using a STM32F3 Discovery board. Two USRs records of 1 kSa, digitized at a sample rate of 1 MSa/s were considered. The sine-fit cosine and sine coefficients were calculated offline and stored in the microcontroller flash memory, in order to reduce the computation time. The  $\varphi_1$  and  $\varphi_2$  phase components through the sine-fit algorithm, the TDoA and the TDeA algorithms

through Table 2.1. Finally the estimated heading through the eq.(3.11), was computed by the microcontroller.

A throughput of 505 Sa/s was proved with the 85% time effort arising from the sine-fit algorithm and the remaining part mainly from the TDeA and heading calculation.

To make the experimental campaign easier, signals were digitized by using the TDS1002 Tektronix DSO. The sampling rate was fixed at 10 MSa/s for guaranteeing an ENOB compatible with the STM32 Microcontroller. In Table 3.3, the proposed system and other recent state-of-the-art solutions are compared in terms of range, maximum error, and operation distance.



## Chapter 4

# Conclusions

This thesis involved the study of an indoor positioning tracking and heading measurements system, which in recent years have become increasingly relevant in the different fields of research and development. The importance of this topic is linked to the fact that most of the recent applications are based on a high level human interaction with the electronic devices. The user position in real time and with a low-cost solution (e.g. Augmented Reality, Virtual Reality, Robot Navigation) must be known here. Different positioning techniques and solutions were investigated to understand the trade-off in the current solution. The most important characteristics of a localization system are the accuracy and the latency. Usually, the accuracy range in indoor localization application varies from meter range to sub-centimetre range. The best solution in terms of latency and accuracy is offered by the infrared camera combined with infrared reflective markers. Thanks to the high refresh rate camera, low latencies (1 ms) can be reached. Unfortunately, this solution is very expensive and its cost is only justified in some cases (e.g. military application).

Merge different technologies offer vantages in terms of cost and performance. In this work, the ultra-wide-band and ultrasonic technologies were merged to get the benefit from each technology. The positioning system based on the ultrasonic technology offers good latency (20-100 ms) and accuracy performances (10-20 cm). A preliminary prototype tracking system based on ultrasonic ranging measurements and time difference of arrival was developed, but this solution was discarded because of some issues during testing. The principal problems were the beacons-

target line of sight requirements and the multi-path. Both of these issues are questioned in literature. The solution required is an increase of the number of sensors and time synchronization between them. For these reasons, the ultra wide band technology was chosen for the positioning systems realization.

The commercial module *Decawave DWM100* offers 10 cm ranging measurements accuracy. This module is a low-cost system based on an integrated ultra-wide-band antenna and an on-board ASIC for the measurements. The modules were used as ranging measurements system combined with an extended Kalman filter to compute the target position information. The position information is needed also to measure the heading of the target because the proposed heading systems need to know the relative position with respect to the heading reference beacon.

The traditional heading systems are based on the IMU. The IMU solution offers good performance at a reasonable cost. In order to obtain the heading measurements, the IMU needs a magnetometer sensor. In the presence of a magnetic field disturbance, the magnetometer can not be used. The proposed heading measurements system was based on ultrasonic phase-difference measurements. The ultrasonic technologies don't suffer of the magnetic interference's and can be used in the presence of magnetic disturbances.

The proposed phase-difference measurements method, uses the standard sine-fit algorithm in order to extract the phase shifting. The heading ultrasonic heading measurements, with respect to the positioning measurements, was less sensitive to the multipath phenomena. The interference analysis study explains the limit of the proposed solution. The line-of-sight issues can be solved if more ultrasonic emitters are added with synchronization. With respect to the positioning system, the synchronization doesn't affect the accuracy.

The ultrasonic heading system was fully prototyped and metrologically characterized. A maximum deterministic error of 1.2 degrees with  $1-\sigma$  repeatability of 0.8 degrees, is comparable with the state of the art magnetometer-based heading systems [77, 75]. During the research, a low cost goniometer was developed in order to validate the proposed heading system with a deterministic error of 0.70 degrees and  $1-\sigma$  repeatability of 0.06 degrees.

The UWB system was prototyped, but only the simulation phase was studied. The simulation phase suggests the usage of a sensor fusion

strategy with IMU data, in order to reduce the noise in the position measurements for the  $\beta_{bias}$  estimation [111, 112, 113].

In addition to that, the ultrasonic heading system can be fused with the IMU data in order to obtain the fully orientation tracking. Thanks to the proposed heading system, a magnetometer less IMU architecture can be used. Introducing a third ultrasonic sensor, even the pitch can be estimated and the distance between the ultrasonic emitter. The information from the IMU, the UWB system, and the ultrasonic measurements, can be fused together in order to increase the accuracy and the system robustness.

More investigation is needed for the UWB system and the ultrasonic heading with the IMU system integration.



# Bibliography

- [1] Benjamin Wagner, Tobias Ritt, and Dirk Timmermann. Multiple user recognition with passive rfid tomography. In *Positioning, Navigation and Communication (WPNC), 2014 11th Workshop on*, pages 1–6. IEEE, 2014.
- [2] D Capriglione, D Casinelli, and L Ferrigno. Use of frequency diversity to improve the performance of rssi-based distance measurements. In *Measurements & Networking (M&N), 2015 IEEE International Workshop on*, pages 1–6. IEEE, 2015.
- [3] Valter Pasku, Alessio De Angelis, Marco Dionigi, Guido De Angelis, Antonio Moschitta, and Paolo Carbone. A positioning system based on low-frequency magnetic fields. *IEEE Transactions on Industrial Electronics*, 63(4):2457–2468, 2016.
- [4] Lionel M Ni, Yunhao Liu, Yiu Cho Lau, and Abhishek P Patil. Landmarc: indoor location sensing using active rfid. *Wireless networks*, 10(6):701–710, 2004.
- [5] Bernd Schleicher, Ismail Nasr, Andreas Trasser, and Hermann Schumacher. Ir-uwband radar demonstrator for ultra-fine movement detection and vital-sign monitoring. *IEEE transactions on microwave theory and techniques*, 61(5):2076–2085, 2013.
- [6] Nissanka Bodhi Priyantha. *The cricket indoor location system*. PhD thesis, Massachusetts Institute of Technology, 2005.
- [7] Eric A Wan and Anindya S Paul. A tag-free solution to unobtrusive indoor tracking using wall-mounted ultrasonic transducers. In *Indoor Positioning and Indoor Navigation (IPIN), 2010 International Conference on*, pages 1–10. IEEE, 2010.

- 
- [8] Sérgio I Lopes, José MN Vieira, João Reis, Daniel Albuquerque, and Nuno B Carvalho. Accurate smartphone indoor positioning using a wsn infrastructure and non-invasive audio for tdoa estimation. *Pervasive and Mobile Computing*, 20:29–46, 2015.
- [9] Tobias Schroeder. An accurate magnetic field solution for medical electromagnetic tracking coils at close range. *Journal of Applied Physics*, 117(22):224504, 2015.
- [10] Prowave. 250st160, 2013. original document from Prowave.
- [11] Knowles. Spu0410lr5h-qb, 2013. original document from Knowles Electronics.
- [12] Isaac Amundson and Xenofon D Koutsoukos. A survey on localization for mobile wireless sensor networks. In *International Workshop on Mobile Entity Localization and Tracking in GPS-less Environments*, pages 235–254. Springer, 2009.
- [13] Giulia Piovan, Iman Shames, Barış Fidan, Francesco Bullo, and Brian DO Anderson. On frame and orientation localization for relative sensing networks. *Automatica*, 49(1):206–213, 2013.
- [14] Michael Aron, Gilles Simon, and Marie-Odile Berger. Use of inertial sensors to support video tracking. *Computer Animation and Virtual Worlds*, 18(1):57–68, 2007.
- [15] Tingyu Zhao, Chung-Ming Own, and Chao Xu. 3d positioning information on augmented identification for indoor localization. In *Proceedings of the 2nd International Conference on Communication and Information Processing*, pages 216–221. ACM, 2016.
- [16] Hirokazu Kato and Mark Billinghurst. Marker tracking and hmd calibration for a video-based augmented reality conferencing system. In *Augmented Reality, 1999.(IWAR'99) Proceedings. 2nd IEEE and ACM International Workshop on*, pages 85–94. IEEE, 1999.
- [17] A Seshanka Venkatesh, K Vamsi Krishna, NKR Swamy, and P Simhachalam. Robot navigation system with rfid and ultrasonic sensors. *International Journal of Engineering Research & Science (IJOER)*, 2.

- 
- [18] Torry Kho, Muataz H Salih, Yan San Woo, Zheng Ng, Janice Jia Min, and Fengjie Yee. Enhance implementation of embedded robot auto-navigation system using fpga for better performance. In *Electronic Design (ICED), 2016 3rd International Conference on*, pages 309–314. IEEE, 2016.
- [19] Sivanand Krishnan, Pankaj Sharma, Zhang Guoping, and Ong Hwee Woon. A uwb based localization system for indoor robot navigation. In *Ultra-Wideband, 2007. ICUWB 2007. IEEE International Conference on*, pages 77–82. IEEE, 2007.
- [20] Alberto Serra, Davide Carboni, and Valentina Marotto. Indoor pedestrian navigation system using a modern smartphone. In *Proceedings of the 12th international conference on Human computer interaction with mobile devices and services*, pages 397–398. ACM, 2010.
- [21] Haoran Ma, Jinliang Liao, Xiao Chen, and Alan Zhang. ilost–bluetooth indoor navigation system. 2016.
- [22] María Martínez Pérez, Mariano Cabrero-Canosa, José Vizoso Hermida, Lino Carrajo García, Daniel Llamas Gómez, Guillermo Vázquez González, and Isabel Martín Herranz. Application of rfid technology in patient tracking and medication traceability in emergency care. *Journal of medical systems*, 36(6):3983–3993, 2012.
- [23] T Dylan McAllister, Samy El-Tawab, and M Hossain Heydari. Localization of health center assets through an iot environment (locate). In *Systems and Information Engineering Design Symposium (SIEDS), 2017*, pages 132–137. IEEE, 2017.
- [24] Haiming Cheng, Ling Huang, He Xu, Yifan Hu, and Xu An Wang. Design and implementation of library books search and management system using rfid technology. In *Intelligent Networking and Collaborative Systems (INCoS), 2016 International Conference on*, pages 392–397. IEEE, 2016.
- [25] Prachya Kamol, Stefanos Nikolaidis, Ryuichi Ueda, and Tamio Arai. Rfid based object localization system using ceiling cameras with particle filter. In *Future generation communication and networking (fgcn 2007)*, volume 2, pages 37–42. IEEE, 2007.

- 
- [26] Wonho Kang and Youngnam Han. Smartpdr: Smartphone-based pedestrian dead reckoning for indoor localization. *IEEE Sensors journal*, 15(5):2906–2916, 2015.
- [27] Shuopeng Wang, Peng Yang, and Hao Sun. Fingerprinting acoustic localization indoor based on cluster analysis and iterative interpolation. *Applied Sciences*, 8(10):1862, 2018.
- [28] Marco Altini, Davide Brunelli, Elisabetta Farella, and Luca Benini. Bluetooth indoor localization with multiple neural networks. In *IEEE 5th International Symposium on Wireless Pervasive Computing 2010*, pages 295–300. IEEE, 2010.
- [29] Margrit Betke and Leonid Gurvits. Mobile robot localization using landmarks. *IEEE transactions on robotics and automation*, 13(2):251–263, 1997.
- [30] João Sena Esteves, Adriano Carvalho, and Carlos Couto. Generalized geometric triangulation algorithm for mobile robot absolute self-localization. In *2003 IEEE International Symposium on Industrial Electronics (Cat. No. 03TH8692)*, volume 1, pages 346–351. IEEE, 2003.
- [31] Richard B Langley et al. Dilution of precision. *GPS world*, 10(5):52–59, 1999.
- [32] Heiko Will, Thomas Hillebrandt, and Marcel Kyas. The fu berlin parallel lateration-algorithm simulation and visualization engine. In *2012 9th Workshop on Positioning, Navigation and Communication*, pages 131–136. IEEE, 2012.
- [33] Zang Li, Wade Trappe, Yanyong Zhang, and Badri Nath. Robust statistical methods for securing wireless localization in sensor networks. In *Proceedings of the 4th international symposium on Information processing in sensor networks*, page 12. IEEE Press, 2005.
- [34] Domenico Capriglione, Deborah Casinelli, and Luigi Ferrigno. Analysis of quantities influencing the performance of time synchronization based on linear regression in low cost wsns. *Measurement*, 77:105–116, 2016.

- [35] Timothy Claeys, Franck Rousseau, Bernard Tourancheau, and Andrzej Duda. Clock drift prediction for fast rejoin in 802.15.4e tsch networks. In *2017 26th International Conference on Computer Communication and Networks (ICCCN)*, pages 1–9. IEEE, 2017.
- [36] Bin Xu, Guodong Sun, Ran Yu, and Zheng Yang. High-accuracy tdoa-based localization without time synchronization. *IEEE Transactions on Parallel and Distributed Systems*, 24(8):1567–1576, 2012.
- [37] Swarun Kumar, Stephanie Gil, Dina Katabi, and Daniela Rus. Accurate indoor localization with zero start-up cost. In *Proceedings of the 20th annual international conference on Mobile computing and networking*, pages 483–494. ACM, 2014.
- [38] Rajeev Bansal. The far-field: How far is far enough? *Applied Microwave & Wireless*, 11(11):59–60, 1999.
- [39] J David N Cheeke. *Fundamentals and applications of ultrasonic waves*. CRC press, 2016.
- [40] Hsieh-Chung Chen, Tsung-Han Lin, HT Kung, Chit-Kwan Lin, and Youngjune Gwon. Determining rf angle of arrival using cots antenna arrays: A field evaluation. In *MILCOM 2012-2012 IEEE Military Communications Conference*, pages 1–6. IEEE, 2012.
- [41] Jiuqiang Xu, Wei Liu, Fenggao Lang, Yuanyuan Zhang, Chenglong Wang, et al. Distance measurement model based on rssi in wsn. *Wireless Sensor Network*, 2(8):606–611, 2010.
- [42] Harald T Friis. A note on a simple transmission formula. *Proceedings of the IRE*, 34(5):254–256, 1946.
- [43] Guoqiang Mao. *Localization Algorithms and Strategies for Wireless Sensor Networks: Monitoring and Surveillance Techniques for Target Tracking: Monitoring and Surveillance Techniques for Target Tracking*. IGI Global, 2009.
- [44] P Series. Propagation data and prediction methods for the planning of indoor radiocommunication systems and radio local area networks in the frequency range 900 mhz to 100 ghz. *Recommendation ITU-R*, pages 1238–7, 2012.

- 
- [45] AJ Motley, JM Keenan, et al. Radio coverage in buildings. *Bell System Technical Journal (BTSJ)*, 8:19–24, 1990.
- [46] Lisheng Xu, Feifei Yang, Yuqi Jiang, Lei Zhang, Cong Feng, and Nan Bao. Variation of received signal strength in wireless sensor network. In *Advanced Computer Control (ICACC), 2011 3rd International Conference on*, pages 151–154. IEEE, 2011.
- [47] Andrea Goldsmith. *Wireless communications*. Cambridge university press, 2005.
- [48] US Federal Communications Commission et al. Fcc revision of part 15 of the commission’s rules regarding ultra-wideband transmission systems: First report and order. Technical report, technical report, Feb, 2002.
- [49] Chuanying Zhai, Zhuo Zou, Qin Zhou, Jia Mao, Qiang Chen, Hannu Tenhunen, Lirong Zheng, and Lida Xu. A 2.4-ghz ism rf and uwb hybrid rfid real-time locating system for industrial enterprise internet of things. *Enterprise Information Systems*, 11(6):909–926, 2017.
- [50] Roy Want, Andy Hopper, Veronica Falcao, and Jonathan Gibbons. The active badge location system. *ACM Transactions on Information Systems (TOIS)*, 10(1):91–102, 1992.
- [51] Soo-Yong Jung, Swook Hann, and Chang-Soo Park. Tdoa-based optical wireless indoor localization using led ceiling lamps. *IEEE Transactions on Consumer Electronics*, 57(4), 2011.
- [52] Séphane Poujouly, Bernard Journet, and Dominique Miller. Laser range finder based on fully digital phase-shift measurement. In *Instrumentation and Measurement Technology Conference, 1999. IMTC/99. Proceedings of the 16th IEEE*, volume 3, pages 1773–1776. IEEE, 1999.
- [53] Brett R Sorensen, Max Donath, G-B Yang, and Roland C Starr. The minnesota scanner: A prototype sensor for three-dimensional tracking of moving body segments. *IEEE Transactions on Robotics and Automation*, 5(4):499–509, 1989.

- 
- [54] Shahidul Islam, Bogdan Ionescu, Cristian Gadea, and Dan Ionescu. Indoor positional tracking using dual-axis rotating laser sweeps. In *2016 IEEE International Instrumentation and Measurement Technology Conference Proceedings*, pages 1–6. IEEE, 2016.
- [55] Steven M. La Valle. *Virtual reality*. Cambridge University Press, 2017.
- [56] Louis D Fielder. Human auditory capabilities and their consequences on digital-audio converter design. In *Audio Engineering Society Conference: 7th International Conference: Audio in Digital Times*. Audio Engineering Society, 1989.
- [57] Daniele Marioli, Claudio Narduzzi, Carlo Offelli, Dario Petri, Emilio Sardini, and Andrea Taroni. Digital time-of-flight measurement for ultrasonic sensors. *IEEE Transactions on Instrumentation and Measurement*, 41(1):93–97, 1992.
- [58] Yasuhiro Fukuju, Masateru Minami, Hiroyuki Morikawa, and Tomonori Aoyama. Dolphin: An autonomous indoor positioning system in ubiquitous computing environment. *WSTFES*, 3:53, 2003.
- [59] Hong Liu, Ze Yu, Hongbin Zha, Yuexian Zou, and Lin Zhang. Robust human tracking based on multi-cue integration and mean-shift. *Pattern Recognition Letters*, 30(9):827–837, 2009.
- [60] Aljoša Ošep, Alexander Hermans, Francis Engelmann, Dirk Klostermann, Markus Mathias, and Bastian Leibe. Multi-scale object candidates for generic object tracking in street scenes. In *Robotics and Automation (ICRA), 2016 IEEE International Conference on*, pages 3180–3187. IEEE, 2016.
- [61] Andreas Geiger, Philip Lenz, and Raquel Urtasun. Are we ready for autonomous driving? the kitti vision benchmark suite. In *Computer Vision and Pattern Recognition (CVPR), 2012 IEEE Conference on*, pages 3354–3361. IEEE, 2012.
- [62] Du Yong Kim and Moongu Jeon. Data fusion of radar and image measurements for multi-object tracking via kalman filtering. *Information Sciences*, 278:641–652, 2014.

- [63] Erwin Aitenbichler and Max Muhlhauser. An ir local positioning system for smart items and devices. In *Distributed Computing Systems Workshops, 2003. Proceedings. 23rd International Conference on*, pages 334–339. IEEE, 2003.
- [64] Luc Soler, Stéphane Nicolau, Patrick Pessaux, Didier Mutter, and Jacques Marescaux. Augmented reality in minimally invasive digestive surgery. In *Pediatric Digestive Surgery*, pages 421–432. Springer, 2017.
- [65] Petr Vávra, J Roman, Pavel Zonča, Peter Ihnát, Martin Němec, J Kumar, Nagy Habib, and A El-Gendi. Recent development of augmented reality in surgery: a review. *Journal of healthcare engineering*, 2017, 2017.
- [66] Stéphane Nicolau, Luc Soler, Didier Mutter, and Jacques Marescaux. Augmented reality in laparoscopic surgical oncology. *Surgical oncology*, 20(3):189–201, 2011.
- [67] Ken Cai, Rongqian Yang, Qinyong Lin, and Zhigang Wang. Tracking multiple surgical instruments in a near-infrared optical system. *Computer Assisted Surgery*, 21(1):46–55, 2016.
- [68] Elodie Lugez, Hossein Sadjadi, David R Pichora, Randy E Ellis, Selim G Akl, and Gabor Fichtinger. Electromagnetic tracking in surgical and interventional environments: usability study. *International journal of computer assisted radiology and surgery*, 10(3):253–262, 2015.
- [69] Ziv Yaniv, Emmanuel Wilson, David Lindisch, and Kevin Cleary. Electromagnetic tracking in the clinical environment. *Medical physics*, 36(3):876–892, 2009.
- [70] Guido De Angelis, Alessio De Angelis, Antonio Moschitta, and Paolo Carbone. Comparison of measurement models for 3d magnetic localization and tracking. *Sensors*, 17(11):2527, 2017.
- [71] Oliver J Woodman. An introduction to inertial navigation. Technical report, University of Cambridge, Computer Laboratory, 2007.

- [72] Rita Fontanella, Domenico Accardo, Rosario Moriello, Leopoldo Angrisani, and Domenico Simone. An innovative strategy for accurate thermal compensation of gyro bias in inertial units by exploiting a novel augmented kalman filter. *Sensors*, 18(5):1457, 2018.
- [73] Talat Ozyagcilar. Calibrating an ecompass in the presence of hard and soft-iron interference. *Freescale Semiconductor Ltd*, pages 1–17, 2012.
- [74] Demoz Gebre-Egziabher, Gabriel H Elkaim, J David Powell, and Bradford W Parkinson. Calibration of strapdown magnetometers in magnetic field domain. *Journal of Aerospace Engineering*, 19(2):87–102, 2006.
- [75] Ariela Busato, Pavel Paces, and Jan Popelka. Magnetometer data fusion algorithms performance in indoor navigation: Comparison, calibration and testing. In *2014 IEEE Metrology for Aerospace (MetroAeroSpace)*, pages 388–393. IEEE, 2014.
- [76] Ming Ma, Qian Song, Yang Gu, and Zhimin Zhou. Use of magnetic field for mitigating gyroscope errors for indoor pedestrian positioning. *Sensors*, 18(8):2592, 2018.
- [77] Sebastian OH Madgwick, Andrew JL Harrison, and Ravi Vaidyanathan. Estimation of imu and marg orientation using a gradient descent algorithm. In *2011 IEEE international conference on rehabilitation robotics*, pages 1–7. IEEE, 2011.
- [78] Bastian Hartmann, Norbert Link, and Gert F Trommer. Indoor 3d position estimation using low-cost inertial sensors and marker-based video-tracking. In *IEEE/ION Position, Location and Navigation Symposium*, pages 319–326. IEEE, 2010.
- [79] Shaghayegh Zihajehzadeh, Paul K Yoon, and Edward J Park. A magnetometer-free indoor human localization based on loosely coupled imu/uwb fusion. In *2015 37th Annual International Conference of the IEEE Engineering in Medicine and Biology Society (EMBC)*, pages 3141–3144. IEEE, 2015.
- [80] Chian C Ho and River Lee. Real-time indoor positioning system based on rfid heron-bilateration location estimation and imu

- inertial-navigation location estimation. In *2015 IEEE 39th Annual Computer Software and Applications Conference*, volume 3, pages 481–486. IEEE, 2015.
- [81] Aras Yurtman, Billur Barshan, and Barış Fidan. Activity recognition invariant to wearable sensor unit orientation using differential rotational transformations represented by quaternions. *Sensors*, 18(8):2725, 2018.
- [82] Nissanka B Priyantha, Allen KL Miu, Hari Balakrishnan, and Seth Teller. The cricket compass for context-aware mobile applications. In *Proceedings of the 7th annual international conference on Mobile computing and networking*, pages 1–14. ACM, 2001.
- [83] M Parrilla, JJ Anaya, and C Fritsch. Digital signal processing techniques for high accuracy ultrasonic range measurements. *IEEE Transactions on instrumentation and measurement*, 40(4):759–763, 1991.
- [84] Jerome Blair. Sine-fitting software for iee standards 1057 and 1241. In *Instrumentation and Measurement Technology Conference, 1999. IMTC/99. Proceedings of the 16th IEEE*, volume 3, pages 1504–1506. IEEE, 1999.
- [85] Ricardo Queiros, Francisco Correa Alegria, Pedro Silva Girao, and António Cruz Serra. Cross-correlation and sine-fitting techniques for high-resolution ultrasonic ranging. *IEEE Transactions on Instrumentation and Measurement*, 59(12):3227–3236, 2010.
- [86] Rado Lapuh. Estimating the fundamental component of harmonically distorted signals from noncoherently sampled data. *IEEE Transactions on Instrumentation and Measurement*, 64(6):1419–1424, 2015.
- [87] Rado Lapuh. Phase estimation of asynchronously sampled signal using interpolated three-parameter sinewave fit technique, 2010.
- [88] Steven J Tilden, Thomas E Linnenbrink, and Philip J Green. Standard for terminology and test methods for analog-to-digital converters: a case study of utilization of iee-std-1241. *Computer Standards & Interfaces*, 22(2):103–112, 2000.

- [89] Aldo Baccigalupi, Guido d'Alessandro, Mauro D'Arco, and Rosario Schiano Lo Moriello. Least square procedures to improve the results of the three-parameter sine fitting algorithm. *ACTA IMEKO*, 4(2):100–106, 2015.
- [90] Abhisek Ukil, Vishal H Shah, and Bernhard Deck. Fast computation of arctangent functions for embedded applications: A comparative analysis. In *2011 IEEE International Symposium on Industrial Electronics*, pages 1206–1211. IEEE, 2011.
- [91] Leopoldo Angrisani, Pasquale Arpaia, and Daniele Gatti. Fast beacon recognition for accurate ultrasonic indoor positioning. In *2017 IEEE International Workshop on Measurement and Networking (M&N)*, pages 1–5. IEEE, 2017.
- [92] Decawave. Dw1000 datasheet, 2015. original document from Decawave.
- [93] Greg Welch and Gary Bishop. An introduction to the kalman filter. department of computer science, university of north carolina. *ed: Chapel Hill, NC, unpublished manuscript*, 2006.
- [94] Leopoldo Angrisani, Aldo Baccigalupi, and Rosario Schiano Lo Moriello. A measurement method based on kalman filtering for ultrasonic time-of-flight estimation. *IEEE Transactions on Instrumentation and Measurement*, 55(2):442–448, 2006.
- [95] Antonio Ramón Jiménez and Fernando Seco. Comparing decawave and bespoon uwb location systems: Indoor/outdoor performance analysis. In *Indoor Positioning and Indoor Navigation (IPIN), 2016 International Conference on*, pages 1–8. IEEE, 2016.
- [96] John P Deyst, T Michael Sounders, and Otis M Solomon. Bounds on least-squares four-parameter sine-fit errors due to harmonic distortion and noise. *IEEE transactions on instrumentation and measurement*, 44(3):637–642, 1995.
- [97] Luis M Correia, Dietrich Zeller, Oliver Blume, Dieter Ferling, Ylva Jading, István Gódor, Gunther Auer, and Liesbet Van Der Perre. Challenges and enabling technologies for energy aware mobile radio networks. *IEEE Communications Magazine*, 48(11):66–72, 2010.

- 
- [98] Farzad Samie, Lars Bauer, and Jörg Henkel. Iot technologies for embedded computing: A survey. In *2016 International Conference on Hardware/Software Codesign and System Synthesis (CODES+ISSS)*, pages 1–10. IEEE, 2016.
- [99] M Garcia-Rodriguez, J Garcia-Alvarez, Y Yañez, MJ Garcia-Hernandez, J Salazar, A Turo, and JA Chavez. Low cost matching network for ultrasonic transducers. *Physics Procedia*, 3(1):1025–1031, 2010.
- [100] Alessio De Angelis, Antonio Moschitta, Paolo Carbone, Massimo Calderini, Stefano Neri, Renato Borgna, and Manuele Pappucci. Design and characterization of an ultrasonic indoor positioning technique. In *2014 IEEE International Instrumentation and Measurement Technology Conference (I2MTC) Proceedings*, pages 1623–1628. IEEE, 2014.
- [101] AnalogDevices. Ad8031/8032, 2014. original document from Analog Devices.
- [102] AnalogDevices. Ad8601/ad8602/ad8604, 2011. original document from Analog Devices.
- [103] BIPM. Evaluation of measurement data — guide to the expression of uncertainty in measurement, 2008. Original document from BIPM.
- [104] CL Morfey and GP Howell. Speed of sound in air as a function of frequency and humidity. *The Journal of the Acoustical Society of America*, 68(5):1525–1527, 1980.
- [105] Claudio Canali, Giorgio De Cicco, Bruno Morten, Maria Prudenziati, and Andrea Taroni. A temperature compensated ultrasonic sensor operating in air for distance and proximity measurements. *IEEE Transactions on Industrial electronics*, (4):336–341, 1982.
- [106] Aldo Baccigalupi and Annalisa Liccardo. Field programmable analog arrays for conditioning ultrasonic sensors. *IEEE Sensors Journal*, 7(8):1176–1182, 2007.

- 
- [107] Carlos Medina, Antonio Bravo, José Carlos Segura, Santiago Medina, and Ángel de la Torre. Ultrasound-based orientation and location of mobile nodes combining tof and rssi measurements. *International Conference on Indoor Positioning and Indoor Navigation*, 2016.
- [108] Ui-Suk Suh, Yunha Lee, and Won-Sang Ra. Robust bearing angle estimator for low-cost 1-axis gimbaled ultrasonic seeker. In *2017 IEEE 26th International Symposium on Industrial Electronics (ISIE)*, pages 545–551. IEEE, 2017.
- [109] Lingyu Yang, Xiaoke Feng, Jing Zhang, and Xiangqian Shu. Multi-ray modeling of ultrasonic sensors and application for micro-uav localization in indoor environments. *Sensors*, 19(8):1770, 2019.
- [110] Xiaoke Feng, Lingyu Yang, Jing Zhang, and Yuhan Mou. Research on mav indoor localization and yaw estimation algorithm based on onboard ultrasonic sensors. In *2019 Chinese Control Conference (CCC)*, pages 4147–4154. IEEE, 2019.
- [111] Taehee Lee, Joongyou Shin, and Dongil Cho. Position estimation for mobile robot using in-plane 3-axis imu and active beacon. In *2009 IEEE International Symposium on Industrial Electronics*, pages 1956–1961. IEEE, 2009.
- [112] Ran Liu, Chau Yuen, Tri-Nhut Do, Dewei Jiao, Xiang Liu, and U-Xuan Tan. Cooperative relative positioning of mobile users by fusing imu inertial and uwb ranging information. In *2017 IEEE International Conference on Robotics and Automation (ICRA)*, pages 5623–5629. IEEE, 2017.
- [113] Leehter Yao, Yeong-Wei Andy Wu, Lei Yao, and Zhe Zheng Liao. An integrated imu and uwb sensor based indoor positioning system. In *2017 International Conference on Indoor Positioning and Indoor Navigation (IPIN)*, pages 1–8. IEEE, 2017.